Review | Open Access

Energy Z

Wang *et al. Energy Z* **2026**, *2*, 200018 **DOI:**10.20517/energyz.2026.20

Critical advances in charge separation regulation for photocatalytic CO_2 reduction

Jing Wang[1,*], Chunyu Wang[1], Chaojie Fan[1], Haiyan Liu[1], Jianli Cheng[2,*], Hui Ying Yang[3,*]

Keywords:
Photocatalytic CO_2 reduction, charge separation, heterojunction

Citation: Wang, J.; Wang, C.; Fan, C.; Liu, H.; Cheng, J.; Yang, H. Y. Critical advances in charge separation regulation for photocatalytic CO_2 reduction. *Energy Z* **2026**, *2*, 200018. https://dx.doi.org/10.20517/energyz.2026.20

Received: 21 Apr 2026 **First Decision:** 10 Jun 2026 **Revised:** 16 Jul 2026 **Accepted:** 28 Jul 2026 **Published:** 10 Sep 2026

Academic Editors: Yuping Wu, Jingshan Luo **Copy Editor:** Shu-Yuan Duan **Production Editor:** Shu-Yuan Duan

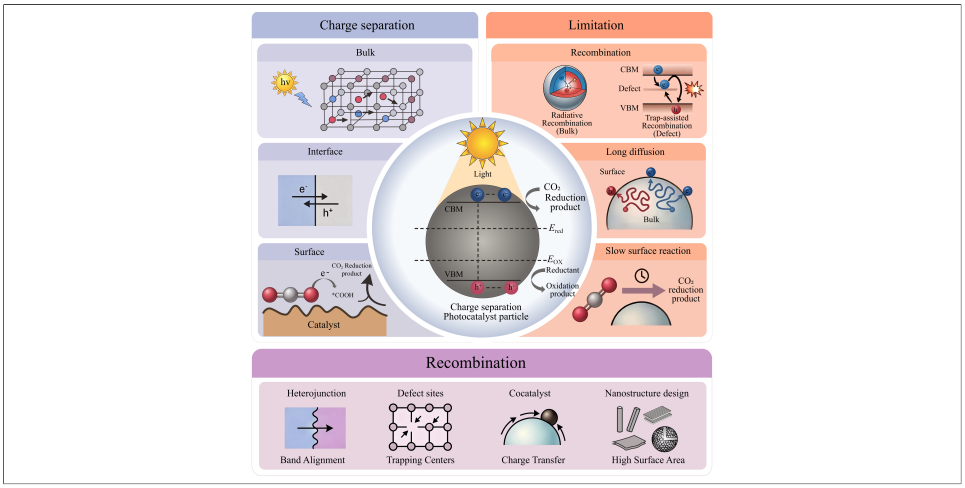

Abstract

The photocatalytic CO_2 reduction (PCR) technology mimics the energy conversion process of natural photosynthesis. PCR is an important strategy to help achieve the future "dual carbon" goals due to its significant advantages of being green, clean, and sustainable. However, the current PCR technology still has a large gap from practical industrial application owing to key problems such as low CO_2 conversion efficiency, poor product selectivity, and insufficient photocatalyst stability. The fundamental reason is the low charge separation efficiency, which is also the core bottleneck restricting performance improvement. This review first outlines the basic mechanism of PCR and systematically analyzes the physical essence of charge separation processes at spatial scales. It further sorts out the internal and external factors that limit the charge separation efficiency, as well as the common techniques and evaluation standards for characterizing charge behavior. It also highlights representative progress in boosting charge separation efficiency through

[1]School of Energy Science and Engineering, Nanjing Tech University, Nanjing 211816, Jiangsu, China.
[2]School of Optoelectronic Science and Engineering, University of Electronic Science and Technology of China, Chengdu 611731, Sichuan, China.
[3]Department of Materials Science and Engineering, College of Design and Engineering, National University of Singapore, Singapore 117575, Singapore.

[*]**Correspondence to:** Prof. Dr. Jing Wang, School of Energy Science and Engineering, Nanjing Tech University, Nanjing 211816, Jiangsu, China. E-mail: wjx2015@njtech.edu.cn; Prof. Dr. Jianli Cheng, School of Optoelectronic Science and Engineering, University of Electronic Science and Technology of China, Chengdu 611731, Sichuan, China. E-mail: jianlicheng@uestc.edu.cn; Prof. Dr. Hui Ying Yang, Department of Materials Science and Engineering, College of Design and Engineering, National University of Singapore, Singapore 117575, Singapore. E-mail: yanghuiying@nus.edu.sg

such strategies as heterojunction construction, defect engineering, catalyst regulation, and morphology optimization. This review provides references and inspiration for the rational design of high-performance PCR catalysts.

INTRODUCTION

Since the Industrial Revolution, the excessive use of conventional fossil fuels (coal, oil, and natural gas) has resulted in a continuous increase in CO_2 concentration, which has become a serious challenge for human society[1,2]. If solar energy can be directly used to convert CO_2 into CO, CH_4, CH_3OH, and even C2+ high-value-added hydrocarbons and oxygen-containing chemicals[3], it will be possible to establish a closed loop of "emission reduction-carbon fixation-fuel/chemical production." This would partially replace fossil resources and alleviate the pressure of carbon emissions. Currently, there are numerous methods for CO_2 reduction, including photocatalysis, electrocatalysis, photoelectrocatalysis, biocatalysis, thermal catalysis, and plasma catalysis[1]. Among these methods, photocatalytic CO_2 reduction (PCR) mimics natural photosynthesis by using semiconductor photocatalysts to capture solar energy and drive the direct conversion of CO_2 and H_2O into hydrocarbons[4]. This process relies solely on solar energy as the input and water and CO_2 as feedstocks. Therefore, compared with other CO_2 reduction methods, PCR has prominent advantages of being green, clean, and sustainable. In recent years, with the rapid advancement of valuation standardization and mechanism investigation, the PCR research paradigm has gradually shifted from "material screening" to "mechanism-driven directed design", and has achieved excellent performance.

However, due to some key challenges and drawbacks, PCR technology is currently at the stage of basic research rather than practical application. For instance, under low CO_2 concentrations, mass transfer and surface adsorption efficiencies are poor[5]. Furthermore, the inherent chemical inertness of the CO_2 molecule imposes high energy barriers for its activation and subsequent multi-step proton-coupled electron transfer processes[5]. Lastly, overall photon utilization and quantum efficiencies remain low[5]. The fundamental cause of these apparent problems is the limited photogenerated charge separation in semiconductor photocatalysts, which remains the core bottleneck in the field of PCR[6]. This is manifested in the following two aspects. Firstly, photogenerated electron-hole pairs undergo rapid recombination. After the semiconductor photocatalyst absorbs photons, electron-hole pairs are generated, but over 90% of them are typically subjected to non-radiative recombination within picoseconds to nanoseconds through bulk or surface defects[7], thus failing to participate in the surface catalytic reaction. This causes a significant loss of photogenerated charges. Secondly, the charge transfer resistance is high. For the separated charges that do migrate to the active sites on the catalyst surface, they often face high interface energy barriers, long transfer paths, and slow coupling rates with reactants or intermediates[8], resulting in sluggish charge utilization kinetics. These bottlenecks not only directly reduce CO_2 conversion activity and stability, but also alter the competitive kinetics of the reaction pathways by influencing the formation and accumulation of key intermediates (such as $*CO_2^-$, *COOH, *CO, *and CHO). Therefore, insufficient charge separation of photocatalysts is a key factor restricting the activity, selectivity, and stability of PCR. Addressing this challenge, effective charge separation regulation has become a central focus in research on photocatalytic CO_2 reduction.

To overcome this issue, researchers have proposed various regulation strategies to enhance charge separation and achieve directional transport. There are three typical examples. (1) At the bulk phase level, the charge transfer path is shortened to inhibit the bulk recombination via band engineering, defect/doping regulation, and morphology structure optimization[9]. (2) At the interface level, spatial charge separation is achieved by constructing various heterojunctions (type-II, Z-scheme, S-scheme, *etc.*)[2]. (3) At the surface level, the construction of Schottky junctions, loading of cocatalysts, and design of atomic-scale active sites are

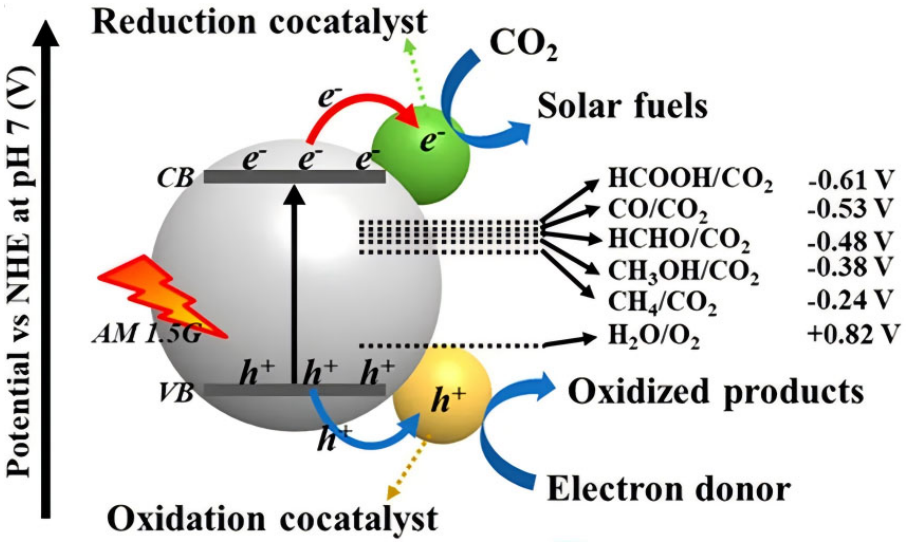

Figure 1. CO_2 conversion by semiconductor photocatalyst. Reprinted from Ref.[11] under the CC BY license. NHE: Normal hydrogen electrode.

employed to achieve efficient coupling between electron extraction and reaction sites, thereby accelerating the adsorption and activation of CO_2 and lowering the energy barrier of rate-determining reaction steps[10]. Especially in recent years, the heterojunction and multi-interface coupling systems emphasize enhancing charge separation while retaining strong oxidation/reduction capabilities, providing a possibility for CO_2 multi-electron deep reduction and C-C coupling.

This review provides a systematic overview of charge separation mechanisms in PCR systems. We first discuss the fundamental principles governing photocatalytic CO_2 reduction and charge carrier dynamics, followed by a detailed analysis of intrinsic and extrinsic factors that limit charge separation efficiency. Subsequently, we summarize representative characterization techniques for probing charge behavior across bulk, interface, and surface scales. Finally, we highlight recent advances in charge separation regulation strategies, including heterojunction engineering, defect modulation, cocatalyst optimization, and morphology design, and provide perspectives on future directions for the rational design of high-performance photocatalysts.

FUNDAMENTAL PRINCIPLES OF CHARGE SEPARATION

Principles of photocatalytic CO_2 reduction

The photocatalytic CO_2 reduction process is governed by three sequential steps: light absorption, charge carrier dynamics, and surface redox reactions, as illustrated in Figure 1. Upon irradiation, the semiconductor photocatalyst absorbs photons with energy equal to or greater than its band gap ($h\nu \geq Eg$). This results in the excitation of electrons from the valence band (VB) to the conduction band (CB), thereby generating electron-hole pairs.

The photogenerated electrons in the CB migrate to the catalyst surface and can be further transferred to a reduction cocatalyst. Here, they participate in the multi-electron reduction of adsorbed CO_2 into solar fuels such as HCOOH, CO, HCHO, CH_3OH, and CH_4[4]. Thermodynamically, this requires the CB minimum to be more negative than the corresponding CO_2 reduction potentials. Meanwhile, the photogenerated holes remaining in the VB migrate to an oxidation cocatalyst to oxidize electron donors (e.g., H_2O or sacrificial agents)[6] into oxidized products, provided that the VB potential is more positive than the oxidation potential.

Therefore, the overall efficiency of photocatalytic CO_2 reduction is synergistically determined by the light absorption capacity, the separation and migration efficiency of photogenerated charge carriers, and the kinetics of surface redox reactions. In particular, efficient charge separation and transfer are critical, as rapid electron-hole recombination during migration severely limits catalytic performance. Consequently, suppressing charge recombination and promoting directional charge transfer are paramount strategies for enhancing the overall PCR efficiency.

Charge separation process

Bulk charge separation

Spatially, charge separation encompasses bulk diffusion to the semiconductor surface and interfacial transfer between different components in composites[12]. In a pristine photocatalyst, the bulk carrier diffusion length critically dictates the efficiency of charge separation and subsequent participation in CO_2 reduction[13]. If the bulk diffusion path is too long, photogenerated electrons will suffer from severe bulk recombination before reaching the active surface sites, rendering even strong light absorption ineffective. Conversely, minimizing the diffusion distance facilitates rapid carrier migration to the active sites. Consequently, engineering low-dimensional nanostructures or hierarchical porous architectures is a highly effective strategy for optimizing bulk charge separation.

However, the performance of bare photocatalysts remains constrained by rapid bulk charge recombination. To mitigate this, composite photocatalysts are constructed by integrating two semiconductors with appropriately matched energy bands[7]. Based on their relative band alignments, heterojunctions are generally classified into three configurations [Figure 2A]: type-I (straddling gap), type-II (staggered gap), and type-III (broken gap)[14]. In a type-I alignment, both electrons and holes transfer to the narrower-bandgap semiconductor, failing to achieve spatial charge separation. Meanwhile, for a type-III alignment, the extreme band offset renders continuous charge transfer energetically prohibitive. In a type-II heterojunction, electrons migrate to the lower conduction band while holes transfer to the higher valence band. This staggered transfer effectively separates the electron-hole pairs spatially, thereby enhancing photocatalytic performance[2]. However, because electrons accumulate at a less negative conduction band potential, the system's overall reductive driving force is compromised, which significantly limits multi-electron CO_2 reduction kinetics. Alternatively, staggered band structures can facilitate a completely different charge transfer mechanism known as a Z-scheme system, where the charge flow resembles the letter "Z" [Figure 2B]. Depending on the charge-mediating mechanism, Z-scheme systems are classified into traditional (using a redox mediator), all-solid-state (using a solid conductor), and direct Z-scheme (without an intermediate medium) heterojunctions. Compared with traditional Z-scheme and all-solid-state Z-scheme, the direct Z-scheme heterojunction can avoid the selection and shielding effects of electron media and reverse photochemical reactions[14]. In this unique pathway, the photogenerated electrons with weaker reductive capability preferentially recombine with holes possessing weaker oxidative capability. Consequently, the strongly reductive electrons and strongly oxidative holes are preserved in their respective conduction and valence bands. Thus, the direct Z-scheme configuration successfully circumvents the redox potential loss inherent to type-II systems. Therefore, constructing appropriate heterojunctions is a critical strategy for enhancing interfacial and spatial charge separation. XPS is an important means for determining the chemical composition and electronic states of materials[15].

Interface charge separation

Photogenerated charge separation at the interface of composite materials is a critical determinant of both the efficiency and selectivity of CO_2 reduction. A prominent example is the charge transfer mechanism in S-scheme heterojunctions, a concept initially introduced by Xu *et al.* in 2019[15]. An S-scheme system consists of a reducing photocatalyst (RP) and an oxidizing photocatalyst (OP). Upon contact, the difference in their

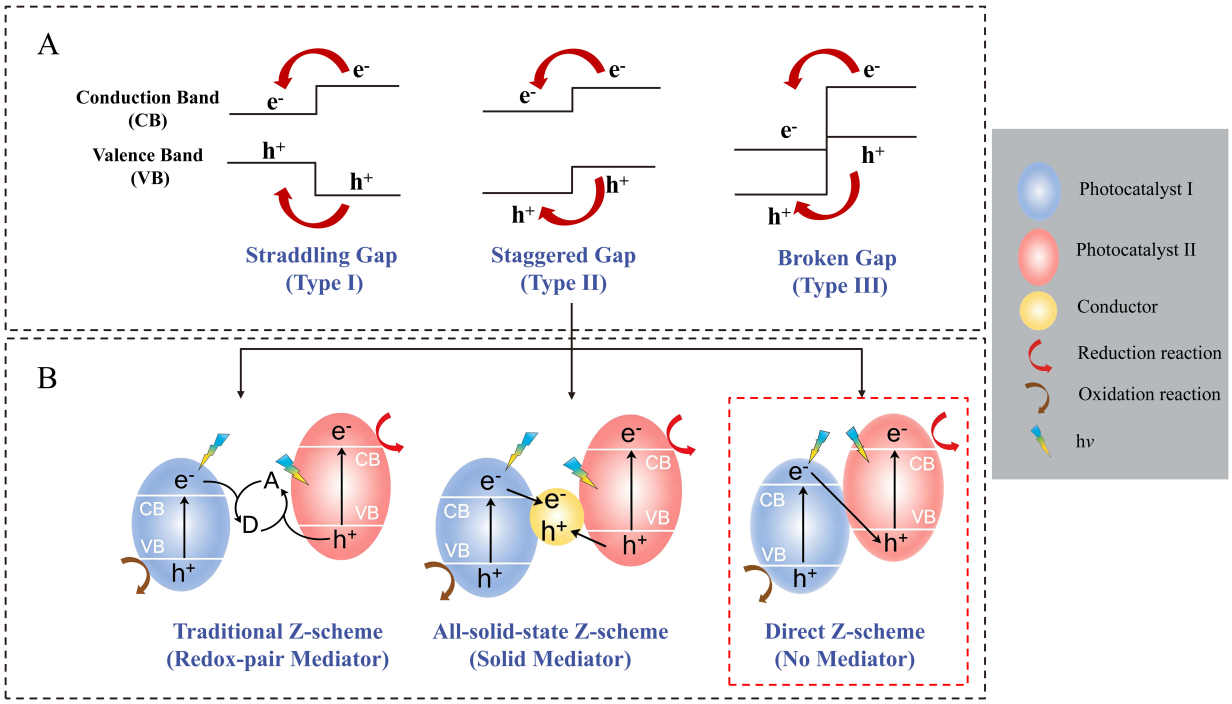

Figure 2. Schematic illustration of typical charge separation paths in two-semiconductor photocatalysts. (A) Band alignment; (B) Z-scheme heterojunctions. Figure 2A and B are adapted from Ref.[14] under the CC BY-NC 3.0 license.

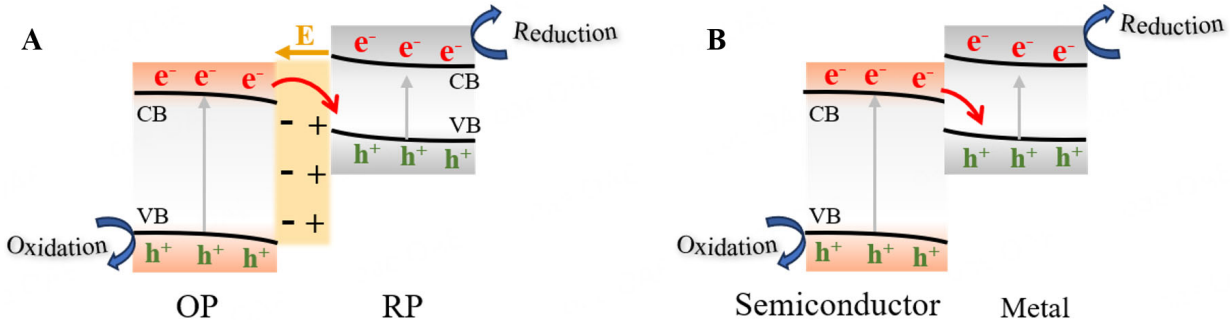

Figure 3. Schematic illustration of typical charge separation paths: (A) S-scheme heterojunction. E is the built-in electric field. (B) Schottky heterojunction. Created with Microsoft PowerPoint. CB: Conduction band; VB: valence band; OP: oxidizing photocatalyst; RP: reducing photocatalyst.

Fermi levels drives spontaneous electron transfer, establishing an internal electric field and inducing corresponding band bending at the interface. Under illumination, this built-in field, synergized with band bending, drives a macroscopic "step-like" interfacial charge transfer pathway [Figure 3A]. This mechanism selectively facilitates the recombination of the less reductive electrons in the OP and the less oxidative holes in the RP. Consequently, the strongly reductive electrons and strongly oxidative holes are preserved in their respective conduction and valence bands. Thus, interfacial charge separation in S-scheme systems is highly directional, achieving efficient carrier separation while maximizing the overall redox potential.

Furthermore, even if photogenerated carriers successfully migrate from the bulk to the semiconductor surface, they remain highly susceptible to rapid recombination if not properly extracted. Therefore, electrons must be further directed across the solid-liquid interface. To achieve this, metallic materials are typically deposited onto the semiconductor surface to form a Schottky junction [Figure 3B][16]. Because the metal generally possesses a larger work function, electrons at the semiconductor surface are preferentially injected

into the metal, which acts as an effective electron trap. Ultimately, these electrons are successfully funneled to the solid-liquid interface, where they participate in the CO_2 reduction reaction on the catalyst surface. The formation of a Schottky barrier subsequently prevents electron backflow, ensuring the strict directionality of surface charge transfer.

Thermodynamic and kinetic parameters of charge separation

In photocatalytic CO_2 reduction, charge separation efficiency is jointly governed by thermodynamic driving forces and kinetic competition[17]. Thermodynamically, this depends on the band alignment between the semiconductor and the CO_2 reduction potentials, which must provide sufficient driving force for the redox reactions while minimizing excessive energy loss[1]. The kinetic competition is primarily determined by the relative charge transfer rate (including interfacial charge injection and transport) and the charge recombination rate (non-radiative recombination in the bulk, surface, and interface)[18]. When the charge transfer rate is significantly higher than the recombination rate, the charge separation efficiency is effectively enhanced. The charge separation efficiency can be expressed as[18]: $\eta_{sep} = \frac{K_{ct}}{K_{ct}+K_{rec}}$, where η_{sep} represents the charge separation efficiency, defined as the fraction of photogenerated electron-hole pairs that are successfully separated and subsequently participate in catalytic reactions. A higher η indicates a greater population of charge carriers effectively involved in catalysis, thereby corresponding to enhanced photocatalytic performance. This parameter fundamentally reflects the dynamic competition between charge transfer and recombination processes. The parameter K_{ct} denotes the charge transfer rate constant, which describes the kinetics of photogenerated carrier migration from the semiconductor bulk or interface to active reaction sites. This encompasses processes such as bulk-to-surface diffusion, carrier injection across semiconductor/cocatalyst interfaces, and electron transfer to adsorbed CO_2 molecules. A larger K_{ct} implies more efficient carrier delivery to catalytic sites, thereby facilitating reaction kinetics. In contrast, K_{rec} represents the charge recombination rate constant, describing the rate at which electrons and holes recombine, including bulk recombination, surface recombination, and interfacial recombination. An increased Krec indicates more severe carrier loss, which is detrimental to photocatalytic efficiency. When K_{ct} is much higher than K_{rec}, the photogenerated charges maintain an effective lifetime in a scale of nanosecond to microsecond. This prolonged lifetime provides a sustained electron supply for the continuous generation of key reactive intermediates (e.g., $*CO_2$ and *COOH). Furthermore, localized internal electric fields, Fermi level alignments, and adsorption-induced dipoles can accelerate interfacial charge injection. These factors enable the rapid transfer of electrons to metal, single-atom, or carbon-based active sites, while holes are concurrently scavenged by strong oxidation centers[17]. This synergistic effect intrinsically suppresses recombination and drastically enhances the overall charge separation efficiency.

Key factors limiting charge separation

The efficiency of charge separation in photocatalytic CO_2 reduction (PCR) is dictated by a combination of both intrinsic and extrinsic factors, which collectively regulate carrier generation, migration, and utilization across the bulk, interface, and surface of photocatalysts[7]. Distinguishing between these two categories is crucial for understanding their respective roles and interdependent effects[17].

Intrinsic factors are primarily dictated by the physicochemical properties of the photocatalyst. At the bulk level, rapid recombination of photogenerated electron-hole pairs represents the primary source of energy loss. In narrow-bandgap semiconductors, high intrinsic carrier densities can exacerbate Coulombic attraction, leading to severe bulk recombination. In addition, deep-level defects and structural disorder introduce trap states that act as non-radiative recombination centers, accelerating carrier annihilation during migration[16]. At the interface level, intrinsic limitations arise from unfavorable band alignment and lattice mismatch. Improper energy level matching between semiconductors or between semiconductors and cocatalysts impedes the formation of a robust built-in electric field, thereby weakening the driving force for

directional charge transfer. Consequently, carriers often recombine at the interface before completing migration[18]. At the surface level, insufficient exposure of active sites or mismatched electronic structures (e.g., inadequate electron affinity) can impede charge utilization. Electrons failing to rapidly inject into adsorbed CO_2 molecules remain highly susceptible to recombination. Concurrently, holes that are not efficiently scavenged by oxidation reactions accumulate at surface states, inducing additional recombination losses[18]. Collectively, these intrinsic constraints severely limit the fraction of charge carriers available for catalytic reactions[10].

In contrast, extrinsic factors stem from external operating conditions and the reaction environment. A primary constraint is restricted light-harvesting capability, particularly in wide-bandgap oxide photocatalysts that respond primarily to ultraviolet light[1]. This limited photon absorption not only curtails the initial generation of charge carriers but also creates a spatial mismatch between the regions of carrier generation and reaction sites, increasing the probability of recombination during migration.

Furthermore, sluggish activation and weak adsorption of CO_2 molecules significantly impede charge utilization. When CO_2 concentration is low or the catalyst-CO_2 interaction is weak, sluggish activation and weak adsorption of CO_2 molecules significantly impede charge utilization (e.g., $*CO_2^-$)[5]. Consequently, accumulated electrons at the interface are more likely to recombine with holes rather than participate in reduction reactions. Because CO_2 reduction is a complex multi-electron transfer process, any disruption can ultimately degrade catalytic activity, product selectivity, and apparent quantum efficiency[1].

Ultimately, intrinsic and extrinsic factors do not operate in isolation; rather, they compound one another to dictate the overall charge separation efficiency. Therefore, effective regulation strategies should simultaneously address material design and reaction conditions to minimize recombination losses and maximize carrier utilization[7].

Characterization techniques for charge behavior

To elucidate the intrinsic mechanisms of charge separation in photocatalytic CO_2 reduction (PCR) systems, it is essential to transcend isolated descriptors and instead consider charge behavior as a continuous physicochemical process spanning photogeneration, carrier migration[19], interfacial redistribution, and surface reaction coupling, as schematically integrated in Figure 4. In this context, characterization techniques should be interpreted in direct correspondence with these successive stages, rather than as independent analytical tools, so as to establish a mechanistically consistent understanding of charge evolution.

At the initial stage of light absorption and carrier generation (Step 1-2 in Figure 4), the dominant process is the competition between carrier excitation and ultrafast recombination in the bulk phase. The absorption characteristics of light can be analyzed through ultraviolet–visible (UV-vis) diffuse reflectance spectroscopy, and the band gap (Eg) value of the photocatalyst can be estimated using the Tauc plot method[20]. Photoluminescence (PL) and time-resolved photoluminescence (TRPL) are therefore commonly employed to probe recombination dynamics. An attenuated PL intensity or prolonged lifetime is often interpreted as indicative of reduced recombination probability[21]. However, such interpretations are inherently limited because PL-based techniques selectively probe radiative recombination pathways and cannot distinguish whether the attenuation of emission arises from improved spatial charge separation or enhanced non-radiative decay via defect states[22]. In addition, TRPL provides only averaged lifetime information and lacks the spatial resolution required to differentiate recombination occurring in the bulk, at the interface, or on the surface. Consequently, although PL and TRPL are useful for preliminary screening, they cannot independently establish the effectiveness of charge separation along the migration pathway depicted in Figure 4. For instance, in a Co_1-C_3N_4@α-Fe_2O_3 Z-scheme photocatalyst, TRPL analysis revealed a prolonged

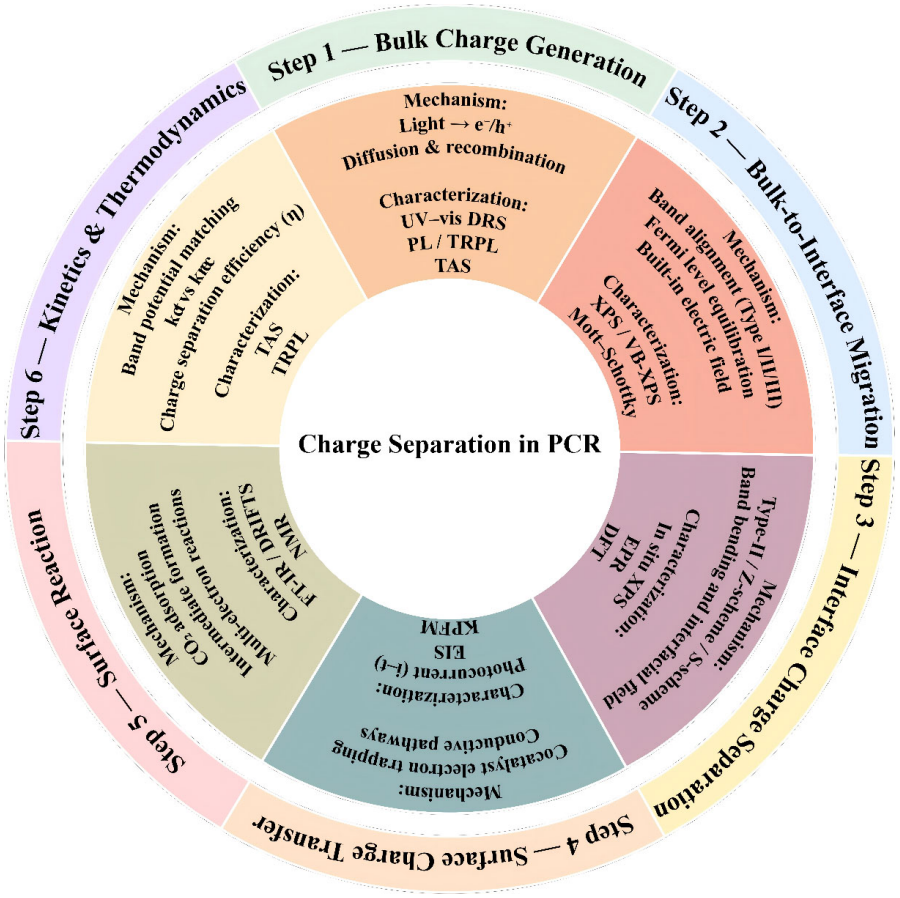

Figure 4. Integrated correlation between charge separation processes and characterization techniques across bulk, interface, and surface levels in PCR systems. Created with Microsoft PowerPoint. PCR: Photocatalytic CO_2 reduction; TAS: transient absorption spectroscopy; TRPL: time-resolved photoluminescence; NMR: nuclear magnetic resonance; FT-IR: Fourier transform infrared spectroscopy; EIS: electrochemical impedance spectroscopy; KPFM: Kelvin probe force microscopy; EPR: electron paramagnetic resonance; DFT: density functional theory; XPS: X-ray photoelectron spectroscopy; VB: valence band; UV-vis: ultraviolet–visible; DRS: diffuse reflectance spectroscopy; PL: photoluminescence.

exciton lifetime after constructing the heterojunction and introducing single-atomic Co sites, indicating that interfacial charge separation and atomic-site regulation synergistically attenuated carrier recombination[23]. This example demonstrates that PL/TRPL can provide preliminary evidence for recombination inhibition, although such signals should still be correlated with non-radiative pathways and spatial charge migration.

As photogenerated carriers migrate from the bulk toward interfaces (Step 2-3 in Figure 4), the efficiency of charge extraction and transport becomes the critical factor governing subsequent reaction steps. Electrochemical techniques, such as transient photocurrent response and electrochemical impedance spectroscopy (EIS), are frequently used to evaluate this process[24]. Enhanced photocurrent is generally associated with improved carrier mobility and extraction efficiency, while reduced charge-transfer resistance inferred from Nyquist plots is often taken as evidence of facilitated interfacial transport. Nevertheless, these electrochemical responses are intrinsically influenced by extrinsic factors, including electrode configuration, electrolyte diffusion, and interfacial capacitance, which complicates their direct correlation with intrinsic charge-transfer pathways. As a result, EIS cannot unambiguously resolve whether the observed improvement originates from genuine directional charge separation or from changes in macroscopic transport properties, and therefore cannot distinguish between different charge-transfer modes embedded in Figure 4, such as type-II versus S-scheme mechanisms[25]. In a Cu_2O@Cu-TCPP heterojunction for CO_2 photoreduction, the

optimized Cu_2O@CP-1 sample exhibited the strongest transient photocurrent response and the smallest EIS semicircle, confirming that the *in situ*-constructed p-n junction effectively promoted charge separation and interfacial transport. This case illustrates that TPC and EIS are useful macroscopic indicators of carrier extraction efficiency and charge-transfer resistance.

To directly capture the dynamic evolution of carriers along the migration-separation pathway (Step 2-4 in Figure 4), transient absorption spectroscopy (TAS) provides a uniquely powerful approach by resolving carrier kinetics across femtosecond-to-microsecond timescales[21]. By tracking the temporal evolution of excited-state species, TAS enables direct observation of carrier trapping, relaxation, and interfacial transfer processes that are otherwise inaccessible by steady-state techniques. For instance, Wang et al. employed femtosecond transient absorption spectroscopy, *in situ* irradiated X-ray photoelectron spectroscopy, and electron paramagnetic resonance to investigate a fibrous Ta_2O_5/Ag_2S S-scheme photocatalyst for diluted CO_2 photoreduction[21]. The TAS results revealed ultrafast decay components corresponding to the selective recombination of low-energy carriers, while long-lived signals were assigned to high-energy electrons retained for reduction reactions, providing direct kinetic evidence for the selective recombination-retention mechanism characteristic of S-scheme charge transfer[26].

While TAS resolves the temporal dimension of charge evolution, direct identification of charge redistribution at heterointerfaces (Step 3-4 in Figure 4) requires operando-level electronic structure characterization. In this regard, *in situ* irradiated X-ray photoelectron spectroscopy (ISIXPS) has emerged as one of the most compelling techniques for validating charge-transfer directionality[27]. Under illumination, shifts in core-level binding energies directly reflect electron accumulation or depletion in different components of a heterojunction, thereby providing real-time evidence of charge migration across interfaces[28,29]. A landmark example is the TiO_2@$ZnIn_2S_4$ photocatalyst reported by Wang *et al.*[28], in which opposite photoinduced binding-energy shifts were observed for the two semiconductors under irradiation, unambiguously confirming directional electron transfer driven by the built-in electric field. This *operando* evidence directly maps onto the interfacial charge-separation process depicted in Figure 4 and has become one of the most widely accepted experimental criteria for distinguishing S-scheme mechanisms from conventional type-II charge-transfer models[28].

At the final stage, where separated charges participate in surface reactions (Step 4-6 in Figure 4), the effectiveness of charge separation must ultimately be evaluated in terms of its coupling with CO_2 adsorption and activation. Kelvin probe force microscopy (KPFM) provides nanoscale mapping of surface potential and work-function distribution, enabling visualization of spatial charge accumulation at active sites and interfaces under illumination[30]. At the nanoscale, KPFM has been used to directly visualize photo-injected electrons in CdS quantum dot-modified cesium tungstate nanosheets. The light-induced surface-potential variation revealed directional electron injection from the photoexcited CdS quantum dots into the metal oxide nanosheets, thereby mapping spatial charge redistribution at the heterointerface[31]. This example demonstrates that KPFM can correlate local work-function changes with charge accumulation regions, providing spatial evidence complementary to spectroscopic and electrochemical analyses. Meanwhile, *in situ* spectroscopic techniques such as DRIFTS and electron paramagnetic resonance (EPR) directly track the formation and evolution of reaction intermediates, including $*CO_2^-$ and *COOH species, thereby linking charge injection to specific elementary reaction steps[32]. These approaches highlight that efficient charge separation, as outlined in Figure 4, only translates into enhanced photocatalytic performance when it is effectively coupled with surface reaction kinetics. At the reaction level, *in situ* DRIFTS and EPR can further connect separated charges with CO_2 activation. In CsBr@$CuBr_2$ and related halogen-defect systems, *in situ* DRIFTS was used to follow the evolution of CO_2-derived intermediates, while EPR-related analysis revealed light-induced defect states that acted as dynamic active sites for CO_2 photoreduction[33]. These observations

establish a mechanistic link between charge trapping, defect-mediated CO_2 activation, and intermediate evolution, thereby providing reaction-level evidence for charge utilization.

Despite the apparent diversity of characterization methods, it is crucial to recognize that each technique probes only a specific segment of the charge evolution pathway illustrated in Figure 4. PL and TRPL primarily reflect recombination behavior in the early stage, electrochemical methods capture macroscopic transport properties during migration, TAS resolves ultrafast carrier kinetics, whereas ISIXPS and KPFM provide direct information on interfacial and spatial charge redistribution. Therefore, reliable identification of charge-transfer mechanisms in PCR systems requires convergent evidence from multiple complementary techniques that collectively reconstruct the full charge separation process from generation to reaction. Recent methodological analyses have further emphasized that operando ISIXPS, ultrafast spectroscopy, and theoretical calculations should be jointly employed to establish a self-consistent charge-transfer framework[27].

Accordingly, the characterization techniques discussed above should not merely be regarded as diagnostic tools but as essential criteria for evaluating the validity of proposed charge-separation models. In the following sections, these methods will be revisited in representative case studies to correlate experimentally validated charge-transfer pathways with photocatalytic performance, thereby establishing a unified framework linking Figure 4 to rational catalyst design.

CHARGE SEPARATION REGULATION STRATEGIES

Heterojunction construction

Heterojunction engineering stands as a paramount strategy for regulating charge separation and directional carrier transport in photocatalytic CO_2 reduction systems. From the perspectives of charge-transfer pathways and band alignment, heterojunctions can be generally categorized into conventional type-II, advanced systems (Z-scheme and S-scheme), and Schottky junctions[34].

Historically, the type-II heterojunction has served as the classical model for achieving spatial separation of photogenerated electrons and holes through staggered band alignment. While this configuration effectively suppresses carrier recombination, it inevitably drives electrons and holes toward lower-energy band edges, precipitating a substantial loss of reduction and oxidation potentials[35]. This inherent trade-off fundamentally limits its applicability in photocatalytic CO_2 reduction, where multi-electron transfer reactions demand robust thermodynamic driving forces.

Consequently, recent studies have progressively shifted from conventional type-II systems toward advanced heterojunction configurations that can simultaneously promote charge separation while preserving high-energy carriers. In this context, Z-scheme and S-scheme heterojunctions achieve the selective recombination of low-energy carriers and the retention of strong redox potentials through distinct interfacial charge-transfer pathways. This represents a paradigm evolution from "separation-dominated" to "energy-preserved" charge regulation. In parallel, Schottky heterojunctions, formed at semiconductor-metal interfaces, provide an alternative route by enabling efficient electron extraction and directional transfer via built-in Schottky barriers. This curtails surface recombination without relying on inter-semiconductor band alignment.

Guided by these considerations, the following sections will focus on Z-scheme, S-scheme, and Schottky heterojunctions as representative advanced models for efficient charge separation and utilization. Meanwhile, the conventional type-II mechanism will serve primarily as a foundational reference framework for understanding the evolution of heterojunction design.

Z-scheme heterojunction

The Z-scheme heterojunction is derived from the "Z-scheme" electron transfer mechanism of natural photosynthesis[36]. Its core advantage lies in achieving efficient separation of photogenerated electrons and holes while retaining high-energy electrons with strong reducing ability and high-energy holes with strong oxidizing ability to the greatest extent[37]. This not only provides sufficient high-energy electron donors for the CO_2 photoreduction reaction but also lays a thermodynamic foundation for multi-step proton-coupled electron transfer (PCET) processes, making it an important design direction for catalytic systems to enhance the performance of CO_2 photoreduction.

Fundamentally, the direct Z-scheme heterojunction is an effective charge-transfer regulation strategy[38], and its fundamental charge transfer mechanism is illustrated in Figure 5A. A typical Z-scheme system couples a semiconductor possessing strong oxidation capabilities (analogous to Photosystem II) with another possessing strong reduction capabilities (analogous to Photosystem I). After the two come into contact, the low-energy electrons in the conduction band of PS I and the low-energy holes in the valence band of PS II will preferentially recombine and be consumed at the interface; ultimately the high-energy electrons with strong reduction ability on the conduction band of PS II (directly used for the activation and reduction of CO_2), and the high-energy holes with strong oxidation ability on the valence band of PS I (used to oxidize sacrificial agents) are retained. This characteristic recombination-retention pathway enables both efficient charge separation and strong redox capability. As shown in Figure 5A, the photogenerated electrons in semiconductor B are excited to its conduction band, while holes remain in the valence band. Meanwhile, semiconductor A undergoes a similar excitation process. The key feature is that the electrons in the conduction band of semiconductor A recombine with the holes in the valence band of semiconductor B at the interface (indicated by the downward arrow in Figure 5A), forming a typical "recombination-retention" pathway. Consequently, the electrons with strong reduction ability are preserved in the conduction band of semiconductor B, while the holes with strong oxidation ability remain in the valence band of semiconductor A. Compared to conventional type-II heterojunctions, this architecture offers two distinct advantages. First, it enhances directional charge transfer, wherein built-in electric fields, Fermi level equilibration, and interfacial barrier effects synergistically suppress bulk carrier recombination. Second, it preserves thermodynamic driving forces by circumventing the transfer of carriers to weakly redox-active band edges. The retained high-energy electrons have a sufficiently negative chemical potential, which can efficiently overcome the highest energy barrier of the first electron injection step in the CO_2 reduction reaction, and at the same time provide sufficient energy support for subsequent multi-electron coupling processes, ensuring the continuous progress of the reduction reaction. For further reduction of CO_2, especially the further hydrogenation of *CO intermediates or C-C coupling and other complex steps, the value of the Z-scheme heterojunction is not limited to the basic charge separation, but is reflected in three key dimensions: Firstly, the precise retention of high-energy active electrons can provide the power for the further reduction steps with high energy barriers; Secondly, promoting the rapid cross-interface charge transfer can reduce energy loss during the migration process; Thirdly, maintaining the high availability of electrons at the interface ensures that there is always an adequate electron supply at the reduction sites.

In 2020, Wang *et al.*[41] reported that the Cu_2O-Pt/SiC/IrO_x composite system achieved the coupled photocatalytic reduction of CO_2 to formic acid (HCOOH) and oxidation of water to oxygen (O_2) through the direct and indirect Z-scheme connection of the reduction and oxidation half-reactions. As illustrated in Figure 5D, the Cu_2O-Pt/SiC/IrO_x system integrates spatially separated reduction and oxidation units, in which Cu_2O-Pt mainly serves as the CO_2 reduction side, while SiC/IrO_x functions as the water oxidation side. The Z-scheme charge-transfer pathway enables the recombination of low-energy carriers while retaining electrons with strong reduction ability for CO_2-to-HCOOH conversion and holes with strong oxidation ability for water oxidation. The enhanced charge separation and utilization efficiency are further supported

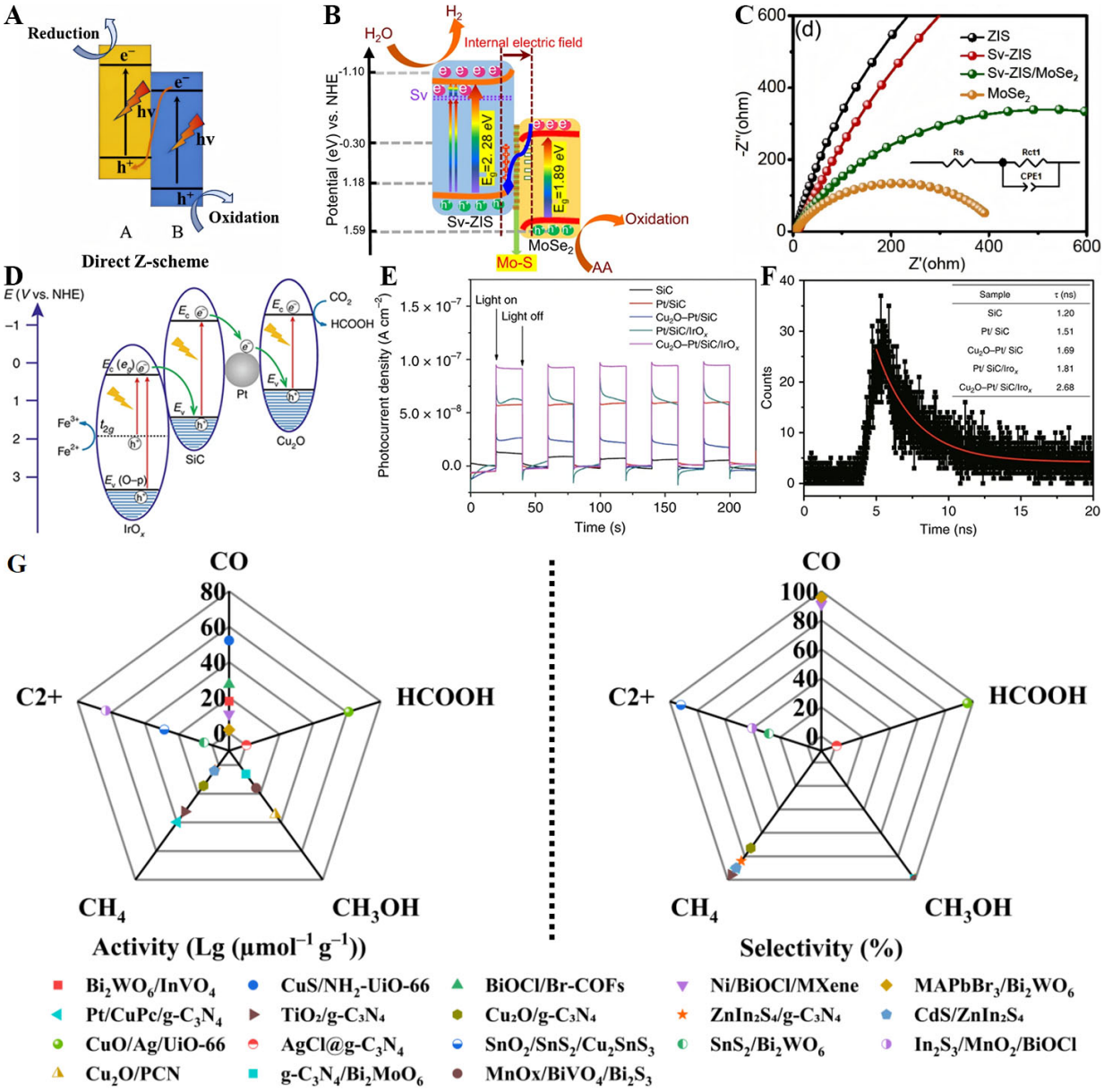

Figure 5. (A) Schematic illustration of charge carrier separation and transfer in a direct Z-scheme heterojunction. Reprinted from Ref.[39] under the CC BY 4.0 license; (B) Schematic illustration of the Z-scheme charge transfer mechanism mediated by interfacial Mo-S chemical bonds; (C) Charge density difference demonstrating electron redistribution at the interface, indicating the role of Mo-S bonds as fast charge transfer channels. Figure 5B and C is reprinted from Ref.[40] under the CC BY 4.0 license; (D-F) Charge transfer pathways and corresponding photocatalytic performance in representative Z-scheme heterojunction systems. Figure 5D-F is reprinted from Ref.[41] under the CC BY 4.0 license; (G) Radar plot comparing catalytic activity (expressed as the logarithm of production rate per mass of catalyst) and selectivity among carbon-containing products. NHE: Normal hydrogen electrode; ZIS: $ZnIn_2S_4$; AA: ascorbic acid.

by Figure 5E and F. The higher HCOOH and O_2 evolution rates indicate that the photogenerated electrons and holes are effectively consumed in the reduction and oxidation half-reactions, respectively. This balanced production behavior suggests that the Z-scheme configuration promotes efficient charge separation and suppresses the reverse reaction, thereby improving the overall photocatalytic CO_2 reduction performance.

Beyond basic composite designs, the integration of multi-component architectures and interface engineering has further amplified Z-scheme performance. In the ternary $ZnFe_2O_4$/ZnO/CdS system, the Z-scheme charge transport path was constructed by controlling the interface structure to achieve efficient carrier separation[42].

The yield of CO_2 to CH_4 was significantly higher than that of single or simple composite systems. The Z-scheme heterojunction constructed through synergy of interface and defect engineering also exhibits remarkable advantages. In the $ZnO/ZnAl_2O_4$ composite, the introduction of oxygen vacancies and interface defects not only improves the interface charge transfer impedance but also promotes the formation of key intermediates (such as *COOH, $*HCO_3^-$), making the conversion performance of CO_2 to CO approximately three times that of pure $ZnAl_2O_4$[43]. At the same time, both the quantum efficiency and the interface charge separation efficiency have been enhanced. This indicates that the Z-scheme interface has a significant effect in enhancing charge directional migration and reaction kinetics. Recently, some novel Z-scheme heterojunctions have been reported. For instance, in Z-scheme CuS/PCN-222 heterojunction, an intimate contact and efficient electron-hole separation were achieved at the interface between CuS and PCN-222, thereby further enhancing the CO_2 reduction activity and carrier utilization rate. This demonstrated the development potential of Z-scheme MOF/sulfide heterojunctions in PCR[44]. Such studies generally indicate that the charge dynamics in Z-scheme heterojunctions can be significantly optimized by regulating the charge separation pathways through interface structure design (such as interface chemical coupling, defect introduction, and multiphase energy level platforms). Beyond constructing intimate interfacial contact, the introduction of interfacial chemical bonding has emerged as a more effective strategy for regulating charge transfer. The formation of covalent or strongly coupled chemical bonds at heterojunction interfaces can not only significantly reduce interfacial charge transfer resistance, but also provide stable and continuous electron transport pathways, thereby enabling more efficient charge separation and directional migration. Recent studies further reveal that interfacial chemical bonding plays a crucial role in charge transfer regulation. As illustrated in Figure 5B and C, the introduction of interfacial bonds (e.g., Mo-S bonds) can establish strong electronic coupling, optimize band alignment, and facilitate directional charge migration. For instance, in a $Bi_{19}S_{27}Br_3$/g-C_3N_4 direct Z-scheme system, the construction of interfacial C-S bonds establishes strong electronic coupling between the two components[45]. This not only accelerates the transfer of photogenerated electrons from g-C_3N_4 to $Bi_{19}S_{27}Br_3$, but also increases interfacial electron density and enhances CO_2 adsorption capability. Although the CO_2 adsorption energy of the $Bi_{19}S_{27}Br_3$/g-C_3N_4 composite is slightly lower than that of pure $Bi_{19}S_{27}Br_3$, this limitation is effectively compensated by the significantly improved charge separation efficiency arising from the Z-scheme heterojunction and interfacial C-S bonds, ultimately leading to markedly enhanced photocatalytic CO_2 reduction performance[45]. Charge density difference analysis further confirms that such interfacial bonds act as efficient charge transfer channels [Figure 5F]. Compared to traditional type-II heterojunctions in which electrons/holes separately migrate to lower energy levels and lose their reduction/oxidation capabilities, the Z-scheme heterojunction effectively retains high-energy carriers and reduces bulk-phase recombination through interface advantages[38], thereby achieving high charge separation efficiency in CO_2 photoreduction reactions and maintaining strong redox driving forces, which is conducive to the complex multi-electron CO_2 reduction (such as the formation of CH_4, C2+ products)[39].

In addition, Figure 5G summarizes the photocatalytic CO_2 reduction performance of representative Z-scheme heterojunctions by correlating activity and product selectivity for the same material systems. The performance parameters were collected from representative studies reported in Refs.[46-62] and further reorganized and visualized by the authors to enable a comparative analysis across different Z-scheme heterojunction systems. The left panel compares the production rates of different reduction products, including CO, CH_4, CH_3OH, and HCOOH, while the right panel presents the corresponding selectivity toward carbon-containing products for each catalyst. This paired comparison shows that Z-scheme heterojunctions not only enhance the overall CO_2 conversion activity but also regulate the product distribution. This unequivocally demonstrates that efficient interfacial charge separation, coupled with the thermodynamic retention of high-energy electrons is the critical determinant in steering the complex reaction pathways of multi-electron CO_2 reduction.

S-scheme heterojunction

In recent years, step-scheme (S-scheme) heterojunctions have rapidly emerged as a focal point in photocatalysis, driven by their unique capacity to regulate interfacial charge transport through a characteristic S-shaped pathway[15]. Typically composed of two semiconductors with distinct work functions[54], the S-scheme architecture leverages this work function differential to drive the formation of an intrinsic electric field. As illustrated in Figure 6A, this internal field, coupled with interfacial band bending and electrostatic potential differences, synergistically establishes the foundation for directional charge migration. Mechanistically, an S-scheme system couples an OP with a RP. Upon illumination, the synergistic driving forces compel photogenerated carriers to follow an S-shaped transport route, where low-energy electrons in the conduction band of the OP preferentially recombine with low-energy holes in the valence band of the RP. Consequently, high-energy electrons with robust reducing capabilities (in the RP) and high-energy holes with potent oxidizing capabilities (in the OP) are selectively preserved and directed to their respective active sites. This selective retention mechanism inherently achieves both spatial charge separation and directional charge transfer. Building upon this concept, dual S-scheme heterojunctions, as illustrated in Figure 6B, further introduce multi-interface coupling to construct cascade built-in electric fields, enabling stepwise directional charge transfer across different interfaces. In such systems, the photogenerated carriers undergo hierarchical recombination of low-energy electrons and holes at multiple junctions, while high-energy electrons and holes are progressively separated and enriched at spatially distinct active sites. This multi-level charge regulation not only enhances charge separation efficiency but also maximizes the preservation of strong redox potentials, thereby offering superior performance in driving multi-electron CO_2 reduction reactions. Ultimately, the defining thermodynamic advantage of the S-scheme heterojunction is its ability to fully preserve the original, highly active band edge positions of the constituent semiconductors. This circumvents the energy level compromises typical of conventional heterojunctions, ensuring that the composite maintains sufficient thermodynamic potential to simultaneously drive both CO_2 reduction and complementary oxidation half-reactions.

Recently, Xu *et al.*[63] reported S-scheme CeO_2/Bi_2S_3 photocatalysis with palladium-catalyzed carbonylation. The CeO_2/Bi_2S_3 system demonstrated a good yield of CO_2 into CO and a high selectivity of approximately 98%, which highlights the comprehensive advantages of the S-scheme structure in enhancing charge separation and product utilization value. Similarly, Zhang *et al.*[64] engineered an interfacial S-scheme heterojunction by anchoring ultrasmall copper phosphosulfide onto 2D g-C_3N_4. Fourier transform infrared (FT-IR) spectroscopy confirmed the formation of interfacial P-N chemical bonds, which act as highly efficient charge transport channels. This synergistic coupling of chemical bonding and S-scheme transport elevated the CO generation rate to eight times that of pristine g-C_3N_4.

Beyond enhancing overall activity, S-scheme heterojunctions demonstrate a remarkable capability to regulate product selectivity in photocatalytic CO_2 reduction. As summarized in Figure 6C, unlike conventional systems where product distribution is primarily dictated by intrinsic material properties, S-scheme architectures fundamentally reshape the reaction kinetics of competing reduction routes.

Because the mechanism selectively preserves high-energy electrons with highly negative potentials, it provides the robust thermodynamic driving force required for complex, multi-electron transfer processes. This ensures a continuous supply of active electrons to drive the formation of deeply reduced species, such as CH_4, CH_3OH, and C2+ hydrocarbons, rather than being limited to two-electron products. Consequently, by finely tuning the band alignment, interfacial electric fields, and catalytic active sites, researchers can effectively modulate the competitive pathways of CO_2 reduction.

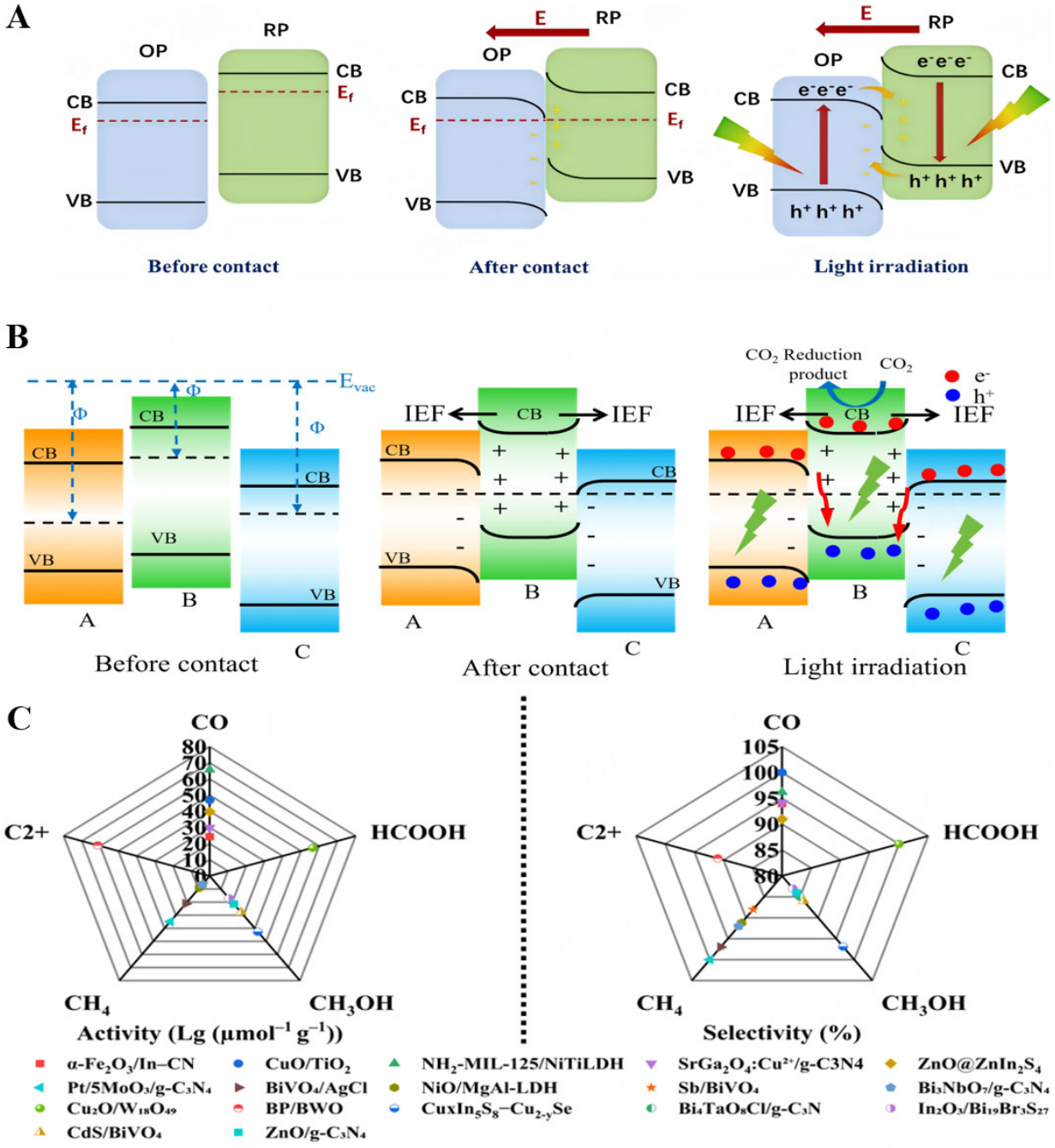

Figure 6. Schematic illustration of the S-scheme heterojunction mechanism: (A) Schematic illustration of the formation mechanism of an S-scheme heterojunction. Reprinted from Ref.[54] under the CC BY 4.0 license; (B) Schematic illustration of dual S-scheme charge carrier transfer process; (C) Radar plot comparing catalytic activity (expressed as the logarithm of production rate per mass of catalyst) and selectivity among carbon-containing products. CB: Conduction band; VB: valence band; IEF: internal electric field.

The product distributions highlighted in Figure 6C provide a comparative overview of the photocatalytic CO_2 reduction performance of representative S-scheme heterojunctions. The catalytic activity and product selectivity parameters were collected from representative studies reported in Refs.[65-81] and further extracted, reorganized, and visualized by the authors to facilitate cross-comparison among different material systems. The comparison indicates that S-scheme heterojunctions exhibit diverse hydrocarbon production capabilities, which are closely associated with the synergistic regulation of charge separation, redox potential retention, and surface reaction kinetics. By promoting the accumulation of high-energy electrons and

stabilizing key intermediates (e.g., *CO and *CHO), S-scheme heterojunctions can facilitate subsequent hydrogenation and C-C coupling processes. These characteristics highlight the potential of S-scheme architectures as versatile platforms for the selective synthesis of value-added solar fuels.

Schottky heterojunction

Schottky heterojunctions are highly effective in enhancing charge separation for photocatalytic CO_2 reduction (PCR). For instance, when a metal contacts an n-type semiconductor [Figure 7A and B][82], the metal's typically higher work function drives spontaneous electron transfer across the interface. To satisfy thermodynamic stability, electrons flow from the semiconductor to the metal until their Fermi levels equilibrate. This interfacial equilibration induces local band bending and establishes a built-in electric field, simultaneously forming a depletion layer within the semiconductor. Consequently, a Schottky barrier emerges at the interface, defined by $\Phi B = \Phi_M - X_{SM}$, where Φ_M represents the work function of the metal and X_{SM} is the electron affinity of the semiconductor. This barrier fundamentally rectifies charge transport by inhibiting the reverse flow of electrons from the metal back to the semiconductor. As a result, the metal acts as a robust "electron sink", facilitating targeted electron accumulation on its surface and effectively suppressing deleterious charge recombination.

These enhanced photocatalytic performances can be attributed to the favorable interfacial electronic interactions in Schottky structures, which facilitate electron transfer and promote surface reaction processes during CO_2 reduction. Crucially, the functional utility of Schottky junctions extends beyond mere charge separation. In PCR systems, the metal component frequently serves as the primary catalytic active site and CO_2 adsorption-activation center, dynamically regulating the adsorption configuration and electronic structure of key intermediates. Furthermore, when plasmonic metals (e.g., Au, Ag) are employed, localized surface plasmon resonance (LSPR) dramatically amplifies optical absorption. This synergistic coupling of hot-electron injection and the Schottky barrier effect fundamentally fortifies interfacial charge separation and modulates product selectivity. These kinetic advantages are thoroughly corroborated by electrochemical characterizations. As illustrated in Figure 7C, the enhanced transient photocurrent response and diminished electrochemical impedance radius collectively signify improved charge separation efficiency and accelerated interfacial transfer dynamics, ultimately elevating overall PCR performance.

Beyond charge transfer kinetics, nuanced interfacial electronic structures and corresponding reaction mechanisms can be elucidated via advanced *in situ* spectroscopy [Figure 7D-F]. X-ray photoelectron spectroscopy (XPS) and extended X-ray absorption fine structure (EXAFS) mapping provide deep insights into the electronic interactions and coordination environments of the metal sites. Complementarily, *in situ* diffuse reflectance infrared Fourier transform spectroscopy (DRIFTS) visualizes the dynamic adsorption and photo-activation of CO_2 molecules[84]. Together, these results substantiate that Schottky metal sites operate dually as efficient electron sinks and active centers for intermediate stabilization.

To further validate the general advantages of Schottky architectures beyond individual case studies, a comprehensive literature comparison was performed [Figure 7G]. The integrated radar plot summarizes the reported photocatalytic CO_2 reduction performance of representative Schottky systems. The integrated radar plot in Figure 7G provides a comparative overview of the reported photocatalytic CO_2 reduction performance of representative Schottky architectures. The catalytic activity and product selectivity parameters were collected from representative studies reported in Refs.[51,83-100] and subsequently extracted, reorganized, and visualized by the authors to enable comparison among different Schottky-type systems and their corresponding single-component counterparts. The comparison indicates that Schottky architectures frequently exhibit enhanced reported catalytic performance, particularly in terms of carbon-containing

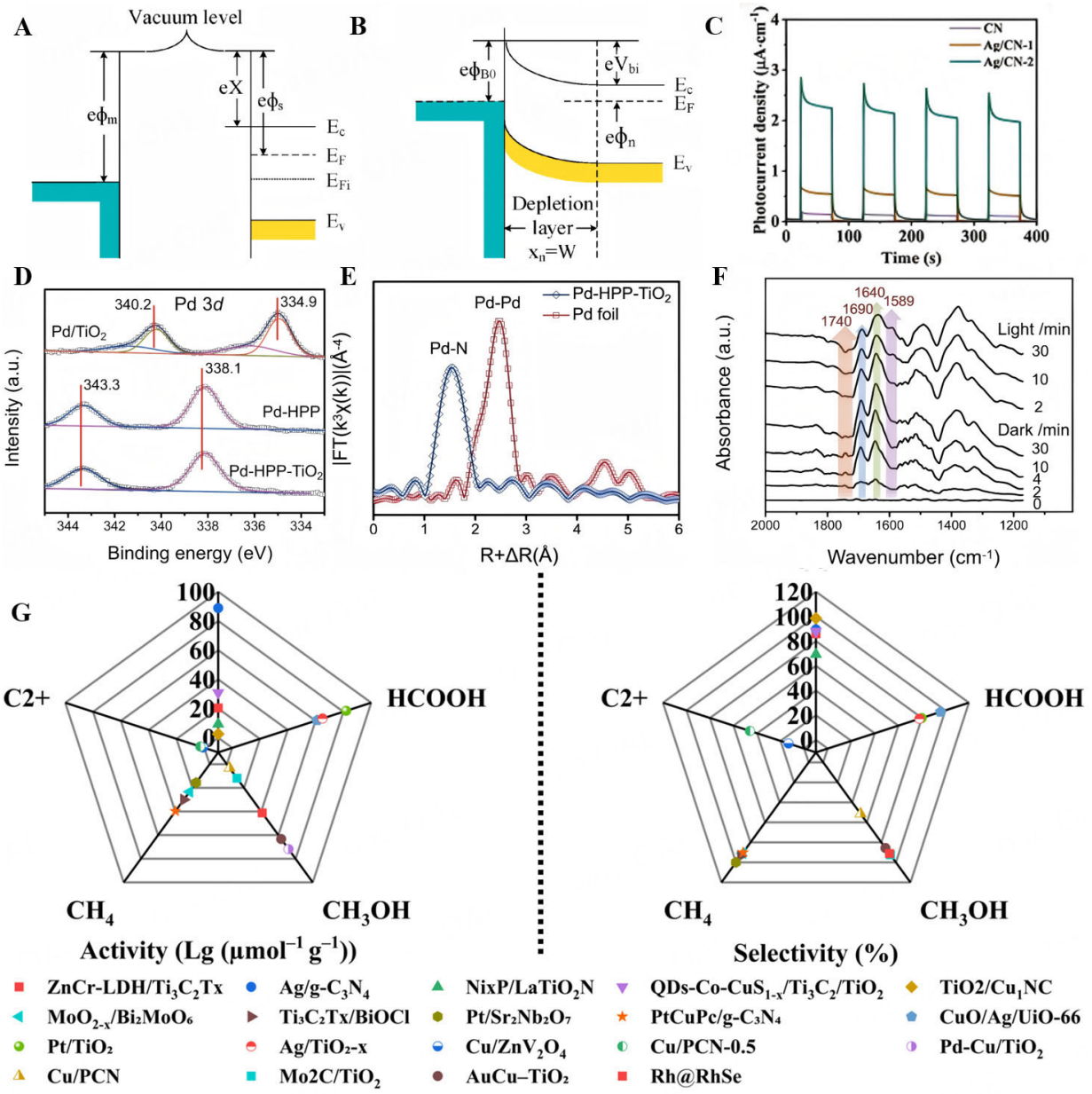

Figure 7. An ideal band diagram of the metal-N semiconductor (A) before contact and (B) after contact. Figure 7A and B is reprinted from Ref.[82] under the CC BY 4.0 license; (C) Transient photocurrent spectra (TPC). Reprinted from Ref.[83] under the CC BY 4.0 license; (D) Comparison of Pd 3d XPS spectra for three photocatalysts; (E) Fourier transformed EXAFS spectra of Pd-HPP-TiO_2 and references; (F) *In situ* DRIFTS test of gas adsorption on Pd-HPP-TiO_2 in the dark and during the photocatalytic CO_2 reduction under UV-visible light irradiation. Figure 7D-F is reprinted from Ref.[84] under the CC BY 4.0 license; (G) Radar plot comparing catalytic activity (expressed as the logarithm of production rate per mass of catalyst) and selectivity among carbon-containing products. XPS: X-ray photoelectron spectroscopy; EXAFS: extended X-ray absorption fine structure; DRIFTS: diffuse reflectance infrared Fourier transform spectroscopy; Pd-HPP-TiO_2: Palladium(II)-coordinated hyper-crosslinked porphyrin-based polymer coated hollow titanium dioxide; UV: ultraviolet.

product formation and selectivity toward specific reduction products, including CO, CH_4, CH_3OH, and HCOOH. These trends can be attributed to the favorable interfacial electronic interactions in Schottky structures, which facilitate electron transfer and may promote surface reaction processes during CO_2 reduction.

Guided by these mechanistic insights, coupling single atoms or highly dispersed nanometals with semiconductors has emerged as a premier strategy for optimizing charge dynamics. For example, in an Ag single-atom anchored TiO_2 system[101], macroscopic electron trapping-induced coloration is harnessed to

Table 1. Comparison of heterojunction architectures for charge separation in photocatalytic CO_2 reduction

Type	Charge separation mechanism	Carrier transfer pathway	Redox capability	Key advantage	Limitation
Z-scheme	Selective recombination of low-energy carriers	High-energy electrons and holes retained in respective bands	Strong	Maintains strong redox ability and improves charge utilization	Requires precise interface design
S-scheme	Built-in electric field-driven selective recombination	Directional recombination via band bending and Fermi level equilibration	Strong	Combines efficient separation with high redox potential	Mechanism identification can be complex
Schottky	Electron extraction via metal-semiconductor interface	Electrons transferred to metal and trapped by Schottky barrier	Strong	Promotes directional electron transfer and suppresses surface recombination	Limited hole utilization and depends on metal properties

bolster electron storage and migration. The isolated Ag atoms act as dominant active sites to stabilize C_1 intermediates, while adjacent Ti sites facilitate H_2O activation for proton supply, culminating in highly selective CH_4 generation[101]. Molecular and polymeric photocatalytic platforms analogously benefit from Schottky junction integration to direct charge flow and maximize surface utilization. In benchmark Ag/g-C_3N_4 systems[102], loading high-work-function metals onto the polymer surface constructs stable Schottky interfaces. This architecture prompts the preferential injection and surface accumulation of photogenerated electrons at the metal sites, severely curtailing bulk-phase recombination and prolonging carrier lifetimes, thereby enhancing the CO production rate significantly beyond that of pristine g-C_3N_4. Moreover, integrating 2D conductive phases, such as MXenes, introduces rapid electron transport channels that augment the interfacial electric field while minimizing contact resistance. For instance, the ZnCr-LDH/$Ti_3C_2T_x$ Schottky system[85], exhibits exceptional CO yield and selectivity under simulated sunlight, validating the dual role of 2D conductive phases in improving electron extraction and reinforcing the Schottky barrier. Additionally, coupling Schottky junctions with defect engineering further amplifies these kinetic efficiencies. In ultrathin SnS_2 layers enriched with sulfur vacancies, the defect sites dramatically expedite proton and electron supply for the complementary water oxidation half-reaction[103]. By synergizing the electron utilization efficiency of the Schottky junction with the enhanced oxidation kinetics of the defect sites, this dual-modulation approach bypasses the kinetic bottlenecks associated with half-reaction mismatches, amplifying the CO generation rate to nearly eight times that of the pristine material. Consequently, contemporary research on Schottky heterojunctions for PCR prioritizes three main trajectories: (i) transitioning from metal nanoparticles to single-atom or atomic-level dispersions to achieve highly efficient electron extraction and precisely defined active sites; (ii) integrating 2D conductive phases as electron transport layers to construct stronger built-in electric fields and minimize interfacial resistance; and (iii) synergizing Schottky architectures with defect engineering to mutually optimize barrier heights, charge separation, and half-reaction kinetic matching. Collectively, these advancements establish Schottky heterojunctions as highly tunable interfacial modules for dictating charge and reaction pathways.

To consolidate this mechanistic landscape, the fundamental characteristics of various heterojunction architectures are summarized in Table 1. The core divergence among these designs lies in their driving forces for charge transfer and the consequent impact on redox potential preservation. Conventional type-II heterojunctions rely on standard band alignment, which ensures spatial separation but inevitably sacrifices critical redox energy. In contrast, both Z-scheme and S-scheme systems employ selective recombination mechanisms that preserve high-energy charge carriers necessary for multi-electron CO_2 reduction. Conversely, Schottky heterojunctions are uniquely driven by work function differentials, establishing robust interfacial barriers that enforce directional electron extraction and maximize charge utilization efficiency.

This progressive evolution from simple band-aligned separation toward advanced, thermodynamics-preserving charge regulation highlights the critical necessity of coupling efficient carrier separation with robust redox potential preservation, aligning perfectly with the overarching charge evolution framework conceptualized in Figure 4.

Defect engineering

Defect engineering focuses on deliberately introducing appropriate lattice defects to precisely regulate the local electronic structure and charge-transfer pathways of semiconductors, thereby achieving highly efficient control over charge capture, storage, and reuse[104]. These defects can induce localized charge density redistribution, modulate band bending, tune built-in electric fields, and dictate the binding affinity and selectivity for surface-adsorbed species. For example, electron-rich defects can enhance molecular adsorption and activate chemical bond bending, thus promoting the formation of critical intermediates (e.g., $*CO_2^-$ and *COOH). Concurrently, hole-trapping centers can suppress non-radiative recombination, ensuring a higher fraction of photogenerated carriers participate in surface catalytic reactions[105]. Furthermore, the localized polarization and electron-rich microenvironments induced by these defects significantly facilitate direct electron transfer to CO_2 molecules. This establishes a highly favorable thermodynamic landscape for subsequent reduction steps, including C-O bond cleavage and C-H bond formation[106]. By systematically regulating defect concentration, type, trap depth, and spatial distribution, researchers can precisely optimize charge capture efficiency, migration pathways, and interfacial reaction kinetics-all without perturbing the intrinsic band edges of the host photocatalyst[107]. Notably, when defect engineering is synergized with complementary strategies, such as interfacial electric field modulation or heterojunction construction, a powerful dual-mechanism emerges: defects serve as localized hubs for electron capture and redistribution, while the enhanced built-in electric field drives rapid, directional charge transfer. Together, these synergistic effects fundamentally elevate overall charge separation and utilization efficiencies in photocatalytic systems.

Vacancy defects

Vacancy defects are one of the most common intrinsic defects in crystalline materials. They refer to the defect formed when lattice nodes lack atoms[108]. Among them, oxygen vacancies (V_O), sulfur vacancies (V_S), and metal vacancies (V_M) are the most representative. In metal oxides (e.g., TiO_2, CeO_2, In_2O_3, ZnO), V_O are typically generated via the detachment of lattice oxygen atoms, leaving behind undercoordinated metal centers and localized electron-rich microenvironments[109, 110]. These localized states serve a dual function: they act as electron-trapping centers that prolong carrier lifetimes by suppressing non-radiative recombination, while simultaneously serving as prime active sites for the adsorption and activation of CO_2 and critical intermediates (e.g., $*CO_2^-$, *COOH)[111]. Advancing beyond empirical observations, recent *in situ* and theoretical studies provide a deeper mechanistic understanding. For example, V_O in CeO_2 induce the formation of active Ce^{3+} species, which lower the energy barrier for the initial single-electron injection into CO_2 via localized charge redistribution[112]. Rather than acting merely as static binding sites, these vacancies function as dynamic electron reservoirs that dictate the spatiotemporal distribution of interfacial electrons. However, excessive vacancy concentrations can introduce deep trap states that inadvertently accelerate charge recombination. Consequently, contemporary research has pivoted from indiscriminately maximizing vacancy density toward the precise tuning of vacancy type, trap depth, and spatial distribution to achieve an optimal synergy between charge dynamics and catalytic activity.

Similarly, sulfur vacancies (V_S) are predominantly engineered in 2D transition metal dichalcogenides and sulfides (e.g., MoS_2, WS_2, and SnS_2). The introduction of V_S breaks local crystalline symmetry, exposing previously inert metal centers and substantially amplifying surface reactivity without perturbing the macroscopic band structure[113]. Recent studies reveal a dual regulatory role for V_S[114]: they introduce shallow defect states that facilitate electron trapping to extend carrier lifetimes, and they trigger an electronic

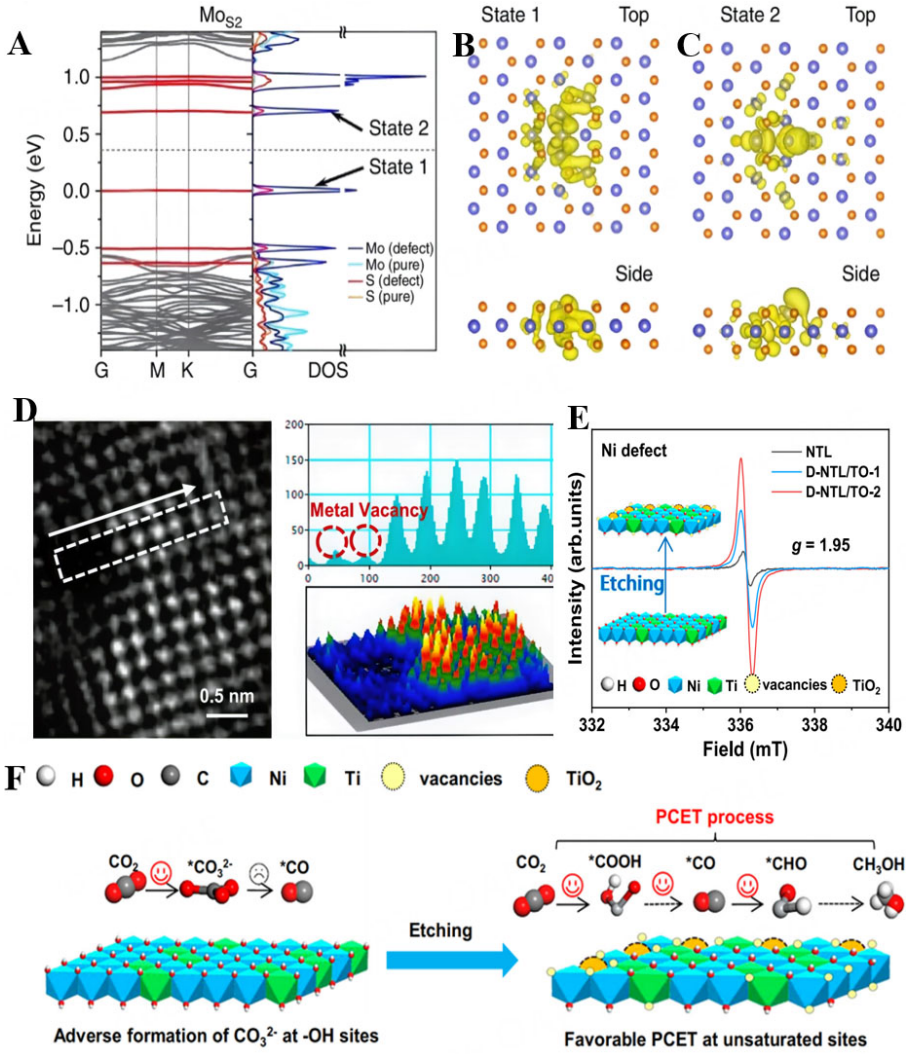

Figure 8. Evidence for vacancy defects in modulating electronic structure and CO_2 reduction pathways: (A) Band structure and corresponding density of states (DOS) of antisite defect MoS_2. The grey bands are from normal lattice sites, similar to conduction band and valence band of perfect monolayer, while the discrete red bands show the localized defects states. The DOS is projected onto the atoms around the defect (defect) and those in the middle plane of two adjacent defects (pure), respectively. The grey dashed line indicates the position of the Fermi Level. (B, C) Real-space distribution of the wave functions of the two defect states below and above the Fermi energy. Figure 8A-C is reprinted from Ref.[113] under the CC BY 4.0 license; (D)AC-TEM image with corresponding 3D surface plot and atomic profile of white-dotted area, and m EDS-STEM element mapping of D-NTL/TO-2. (E)EPR spectra of bulk NTL and acid-etched derivatives. (F) Schematic illustration of the CO_2 activation mechanism on NTL and D-NTL/TO. Figure 8D-F is reprinted from Ref.[115] under the CC BY-NC-ND license. D-NTL/TO: Defective NiTi-layered double hydroxide/titanium dioxide; PCET: proton-coupled electron transfer; AC-TEM: Aberration-corrected transmission electron microscopy; EDS-STEM: energy-dispersive X-ray spectroscopy–scanning transmission electron microscopy; EPR: electron paramagnetic resonance.

reconstruction of adjacent metal atoms, which strengthens CO_2 binding affinity and expedites electron injection. Density of states (DOS) analyses provide direct evidence for this V_S-mediated electronic reconstruction. As depicted in Figure 8A-C, the introduction of V_S generates distinct mid-gap localized states (denoted as State 1 and State 2) originating from the rehybridization of metal d and chalcogen p orbitals. These electron-rich mid-gap states effectively accumulate photogenerated electrons, mitigating rapid recombination and providing an energetically favorable pathway for charge transfer to adsorbed CO_2[113]. Catalytically, these electron-enriched V_S sites promote the back-donation of electrons into the antibonding orbitals of CO_2, accelerating the formation of key intermediates such as $*CO_2^-$ and *COOH. This underscores that sulfur vacancies actively orchestrate interfacial charge transfer and molecular activation rather than functioning as passive electron traps. Consequently, V_S engineering is now a cornerstone design strategy for sulfide-based photocatalytic systems.

In contrast to anion vacancies, metal vacancies (V_M) generally demand higher formation energies, typically requiring harsh annealing or reducing atmospheres, but exert a far more profound impact on the electronic structure and catalytic behavior of the host material[104]. V_M disrupt the local coordination environment, inducing substantial charge redistribution and lattice polarization that enhance both carrier transport and interfacial kinetics. As illustrated in Figure 8D, high-resolution intensity mapping reveals that structurally unsaturated V_M sites trigger pronounced local lattice distortions. These coordination-unsaturated centers induce spatially confined electronic perturbations, fostering charge localization under reaction conditions. This electronic modulation is further corroborated by electron paramagnetic resonance (EPR) spectroscopy [Figure 8E], where a distinct signal at g = 1.95 directly evidences the formation of paramagnetic defect centers associated with Ni vacancies. The intensity evolution of this signal across different treatment conditions highlights that V_M concentration and electronic activity can be dynamically manipulated via post-etching strategies. Catalytically, these V_M-rich domains critically govern adsorption energetics and intermediate evolution. As summarized in Figure 8F, a defective NiTi-TiO_2 system effectively suppresses the formation of thermodynamically stable yet catalytically inert carbonate species, selectively stabilizing the *COOH intermediate, a widely recognized rate-determining precursor for CO_2-to-methanol conversion[115]. This pathway reconfiguration stems from the synergy between V_M-induced electronic state redistribution (enhancing electron availability) and localized geometric distortions (optimizing proton accessibility). Crucially, this modulation transcends static adsorption to actively accelerate PCET kinetics. By shortening the effective distance between charge carriers and intermediates, these unsaturated sites lower the activation barriers for sequential hydrogenation steps (*CO_2 → *COOH → *CO → *CHO). Furthermore, from a carrier dynamics perspective, V_M in metal oxides (e.g., WO_3, TiO_2, Bi_2O_3) decrease the effective mass of holes, thereby boosting their mobility and expediting bulk-to-surface carrier migration[116]. In transition metal oxides like Co_3O_4, V_M promote the formation of high-valence metal species, further driving oxidation kinetics[117]. Thus, metal vacancies operate as multifunctional catalytic motifs that concurrently optimize charge separation, intermediate stabilization, and reaction pathway selectivity.

Ultimately, the formation and behavior of these vacancy defects are intimately governed by the interplay of material composition, crystal structure, and synthetic conditions (e.g., temperature and atmospheric composition). Thermodynamically, vacancy generation must overcome binding-energy-dependent barriers; kinetically, it is dictated by atomic diffusion during thermal or reductive treatments. Table 2 comprehensively summarizes recent advances in vacancy-engineered photocatalysts for PCR. These benchmarks collectively illustrate that whether leveraging V_O in metal oxides, V_S in sulfides, or more complex V_M and dual-defect architectures (V_M + V_S), vacancy engineering remains a paramount strategy. It not only suppresses deleterious charge recombination but also fundamentally dictates the surface reaction pathways and product selectivity in photocatalytic CO_2 reduction.

Doping defects

Doping defects, introduced via the interstitial or substitutional incorporation of metallic or non-metallic heteroatoms, profoundly reconfigure the electronic band structure, local coordination environments, and charge dynamics of host lattices[109]. Unlike intrinsic vacancies, doping provides a highly tunable platform to actively dictate the spatiotemporal behavior of photogenerated carriers and optimize interfacial catalytic performance.

Non-metal dopants (e.g., N, C, S, P, B) primarily modulate the valence band architecture, inducing electronic state reconstruction and generating localized impurity states[106]. Beyond merely broadening the optical absorption spectrum, non-metal doping fundamentally governs interfacial charge transfer. For example, synergistic P-S co-doping transforms polymeric g-C_3N_4 into a narrow-bandgap "black" carbon nitride. This architectural modification not only extends light harvesting into the near-infrared regime but also instigates

Table 2. Summary of vacancy-defect-engineered photocatalysts for CO_2 reduction

Material	Vacancy type	Main product	Light sources	Sacrificial agents	AQE (%)	Rate μmol·g^{-1}·h^{-1}	Ref.
TiO_{2-x}	V_O	CH_4	300 W Xe lamp	H_2O	0.12 (365 nm)	41.8	[118]
Pd/CeO_2	V_O	CO	300 W Xe lamp	H_2O	-	210.9	[119]
$Bi_{12}O_{17}Cl_2$	V_O	CO	300 W Xe lamp	H_2O	-	64.3	[120]
BiOCl	V_O	CO	300 W Xe lamp	H_2O	-	14.51	[121]
BiOBr	V_O	CO	300 W Xe lamp λ ≥ 420 nm	H_2O	-	122.38	[122]
BWO	V_O	CO	300 W Xe lamp	H_2O	0.00394 (500 nm)	18.73	[123]
MoO_{2-x}	V_O	CO	250 W high-pressure mercury lamp	H_2O	-	62.75	[124]
Bi/BiOBr	V_O	CO	200 mW/cm^2 Xe lamp	H_2O	-	251.2	[125]
Bi_2MoO_6@In_2S_3	V_O	CO	300 W Xe lamp λ ≥ 420 nm	H_2O	2.11 (420 nm)	28.54	[126]
ReS_2/CdS	V_S	CO	300 W Xe lamp λ ≥ 420 nm	H_2O	-	7.1	[127]
ZIS	V_S	CO	300 W Xe lamp λ ≥ 420 nm	TEOA	-	61.94	[128]
ZnS/OMNC	V_S	CO	300 W Xe lamp λ ≥ 420 nm	H_2O	-	712.1	[129]
SnS_2	V_S	CO	300 W Xe lamp	H_2O	-	25.71	[103]
Au/CdS-SV	V_S	CO	300 W Xe lamp λ ≥ 400 nm	TEOA	-	12.48	[130]
$ZnIn_2S_4$	V_M	CO	300 W Xe lamp λ ≥ 420 nm	H_2O	2.29 (420nm)	5630	[131]
BiOBr-1	V_M	CO	300 W Xe lamp	H_2O	-	71.23	[132]
VBi-BiOBr	V_M	CO	300 W Xe lamp	H_2O	-	20.1	[133]
$Cu_{1.95}S_{1-x}$	V_M+V_S	CH_4	300 W Xe lamp	H_2O	-	12.42	[134]

AQE: Apparent quantum efficiency; ZIS: $ZnIn_2S_4$; OMNC: ordered mesoporous N-doped carbon; TEOA: triethanolamine.

a redistribution of electron density and local structural polarization, dramatically accelerating CO_2-to-CO conversion by mitigating electron-hole recombination[135].

Conversely, metal ion doping predominantly engineers shallow energy levels near the conduction band and modulates the Fermi level, steering the directional migration of photogenerated carriers. A quintessential example of metal-doping synergy is the Bi-incorporated $In_2O_{3-x}(OH)_y$ system. Here, the strategic construction of surface frustrated Lewis pairs (FLPs, cooperatively regulated by hydroxyl groups and oxygen vacancies) is further optimized by Bi^{3+} substitution at In^{3+} sites. This targeted metal incorporation finely tunes the surface active motifs, dictating both the thermodynamic activation of CO_2 and the ultimate product selectivity[136,137].

Extending these principles, dual-doping strategies (e.g., metal/non-metal combinations or dopant-vacancy couplings) elicit robust synergistic effects. For instance, P-K co-doping in g-C_3N_4 amplifies charge separation while driving the multielectron reduction of CO_2 toward CH_4[138], whereas N-metal co-doping in TiO_2 concurrently broadens spectral responsiveness and enhances product selectivity[139]. Table 3 systematically catalogs recent benchmarks in doping-engineered photocatalysts, highlighting the macroscopic performance gains achieved through these elemental substitutions.

Table 3. Summary of doped photocatalysts for CO_2 reduction

Material	Vacancy type	Main product	Light sources	Sacrificial agents	AQE (%)	Rate $\mu mol \cdot g^{-1} \cdot h^{-1}$	Ref.
TiO_2	N	CO	300 W Xe lamp	H_2O	-	41.1	[140]
TiO_2	N+Eu	CH_4	300 W Xe lamp $\lambda \geq 400$ nm	H_2O	9.1 (350 nm)	13.48	[141]
BiOBr	P	CO	300 W Xe lamp	H_2O	-	9.13	[142]
BiOBr	N	CO	300 W Xe lamp	H_2O	-	18.28	[143]
BiOBr	B	CO	300 W Xe lamp	H_2O	-	21.72	[144]
BiOBr	Co	CO	300 W Xe lamp $\lambda \geq 420$ nm	H_2O	-	11.71	[145]
BiOBr	Eu	CO	300 W Xe lamp	H_2O	-	22.3	[146]
BiOBr-2	Br	CO	300 W Xe lamp	H_2O	-	95.6	[147]
$ZnIn_2S_4$	O	CO	300 W Xe lamp $\lambda \geq 420$ nm	TEOA	-	1680	[148]
$ZnIn_2S_4$	Er	CH_4	300 W Xe lamp $\lambda \geq 420$ nm	TEOA	-	6.68	[149]
$ZnIn_2S_4$	Y	CO	300 W Xe lamp $\lambda \geq 420$ nm	TEOA	0.97 (350 nm)	297.46	[150]
$ZnIn_2S_4$	Yb	CO	300 W Xe lamp $\lambda \geq 420$ nm	TEOA	-	4.59	[151]
CN	P+F	CO	300 W Xe lamp 350 nm $\leq \lambda \leq$ 780 nm	H_2O	-	39.9	[152]
CN	P	CO	300 W Xe lamp	H_2O	-	31.22	[153]
Au/CN	B+K	CO	300 W UV lamp λ = 400 nm	H_2O	-	11.56	[154]
g-C_3N_4	Eu	CH_4	300 W Xe lamp	H_2O	1.6 (420 nm)	22.8	[155]
CN	Cu+P	CO	300 W Xe lamp	H_2O	0.005 (375 nm)	6.01	[156]
Bi_3O_4Br	Co	CO	300 W Xe lamp	H_2O	-	107.1	[157]

AQE: Apparent quantum efficiency; TEOA: triethanolamine.

To bridge these macroscopic catalytic enhancements with atomic-scale charge dynamics, interstitial carbon-doped SnS_2 (SnS_2-C) serves as an elegant mechanistic model [Figure 9A-C]. Interstitial carbon incorporation disrupts local structural symmetry, inducing pronounced lattice microstrain and charge polarization. High-resolution XPS [Figure 9A and B] unveils a distinct positive shift in the binding energies of both Sn 3d and S 2p core levels. This phenomenon signifies partial electron depletion from the host lattice, indicating that interstitial carbon acts as a potent electron-withdrawing locus. Such localized electron redistribution generates a robust built-in electric field that drives the spatial separation of bulk electron-hole pairs, funneling them directionally toward the catalytic interface. Furthermore, as depicted in Figure 9C, the synergy between carbon-induced lattice strain and electronic modulation broadens visible-light harvesting while establishing energetically favorable pathways for charge injection into adsorbed CO_2. Ultimately, this paradigm underscores that doping defect engineering transcends simple bandgap narrowing; it acts as a comprehensive tool to construct internal electric fields, optimize charge routing, and fundamentally dictate the fate of photogenerated carriers at the atomic level.

Cocatalyst modification

Loading cocatalysts on the photocatalyst surface can enhance charge separation, improve charge transfer, or adjust the reaction pathway, thereby improving the overall PCR performance. Generally, cocatalysts are classified into metal cocatalysts and non-metal cocatalysts[109].

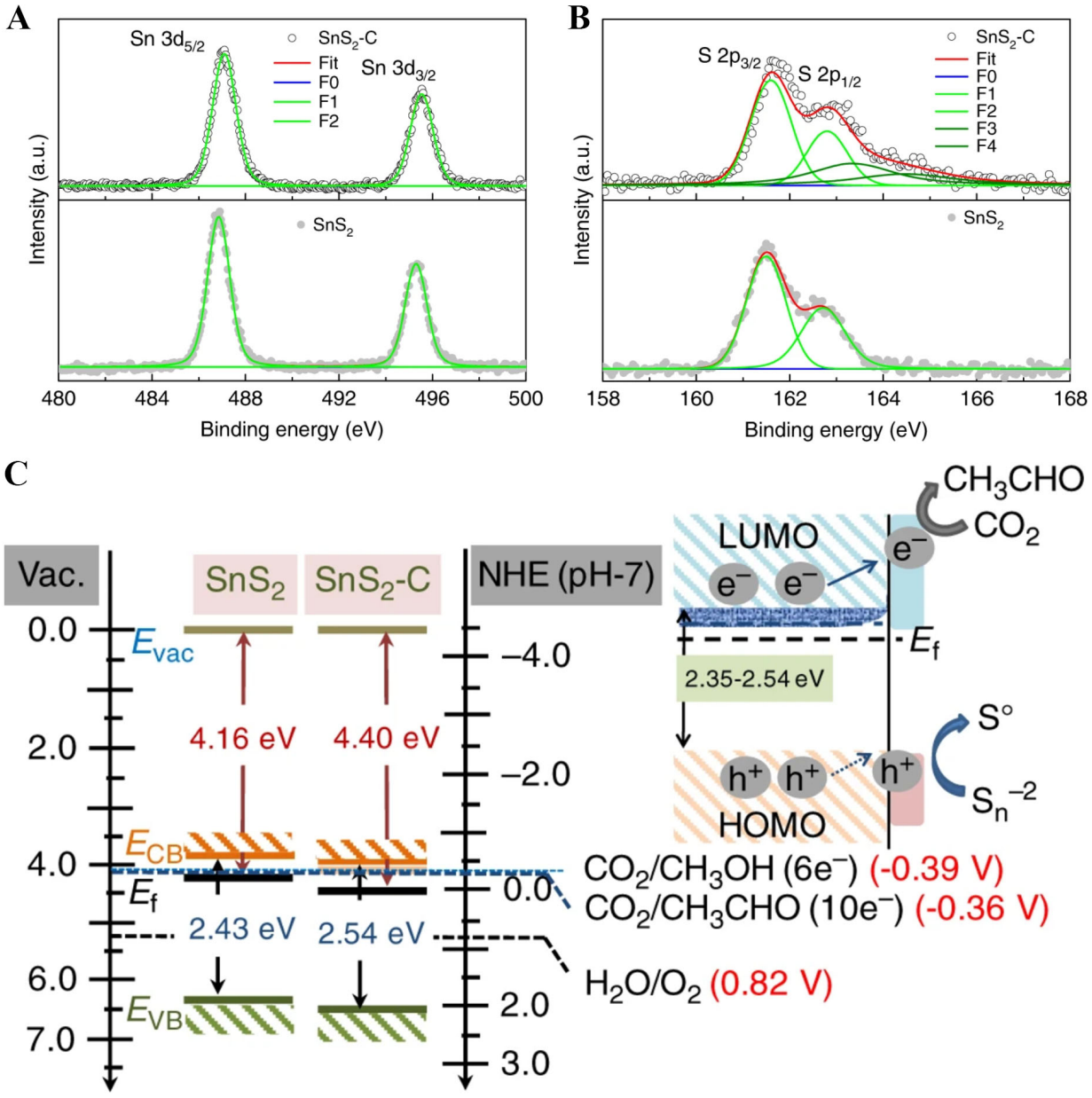

Figure 9. (A) High-resolution XPS Sn 3d spectra of SnS_2-C and SnS_2; (B) High-resolution XPS S 2p spectra of SnS_2-C and SnS_2; (C) Band edge positions and photocatalytic reaction mechanism: Comparative band diagram of SnS_2-C and SnS_2, together with a proposed electron-hole separation of photo-excited electron-hole pairs in SnS_2-C. Figure 9A-C is reprinted from Ref.[158] under the CC BY 4.0 license. SnS_2-C: Carbon-doped SnS_2; CB: conduction band; VB: valence band; NHE: normal hydrogen electrode; LUMO: lowest unoccupied molecular orbital; HOMO: highest occupied molecular orbital; XPS: X-ray photoelectron spectroscopy.

Cocatalysts serve as indispensable structural motifs in photocatalytic systems, bridging the spatial gap between bulk charge separation and interfacial catalytic turnover. Among these, metal nanostructures remain a cornerstone, functioning as potent electron sinks. High-work-function noble metals (e.g., Pt, Au, Pd) equilibrate with the Fermi level of n-type semiconductors upon contact[159], inducing spontaneous band bending and the formation of a robust Schottky junction [Figure 10A]. This built-in potential barrier actively circumvents electron backflow, funneling photogenerated electrons directionally toward the metallic surface where CO_2 reduction transpires. Furthermore, plasmonic cocatalysts (e.g., Ag, Au) harness localized surface plasmon resonance (LSPR) to inject hot electrons directly into the semiconductor conduction band, synergistically amplifying the overall quantum efficiency alongside Schottky-directed charge extraction[102,159].

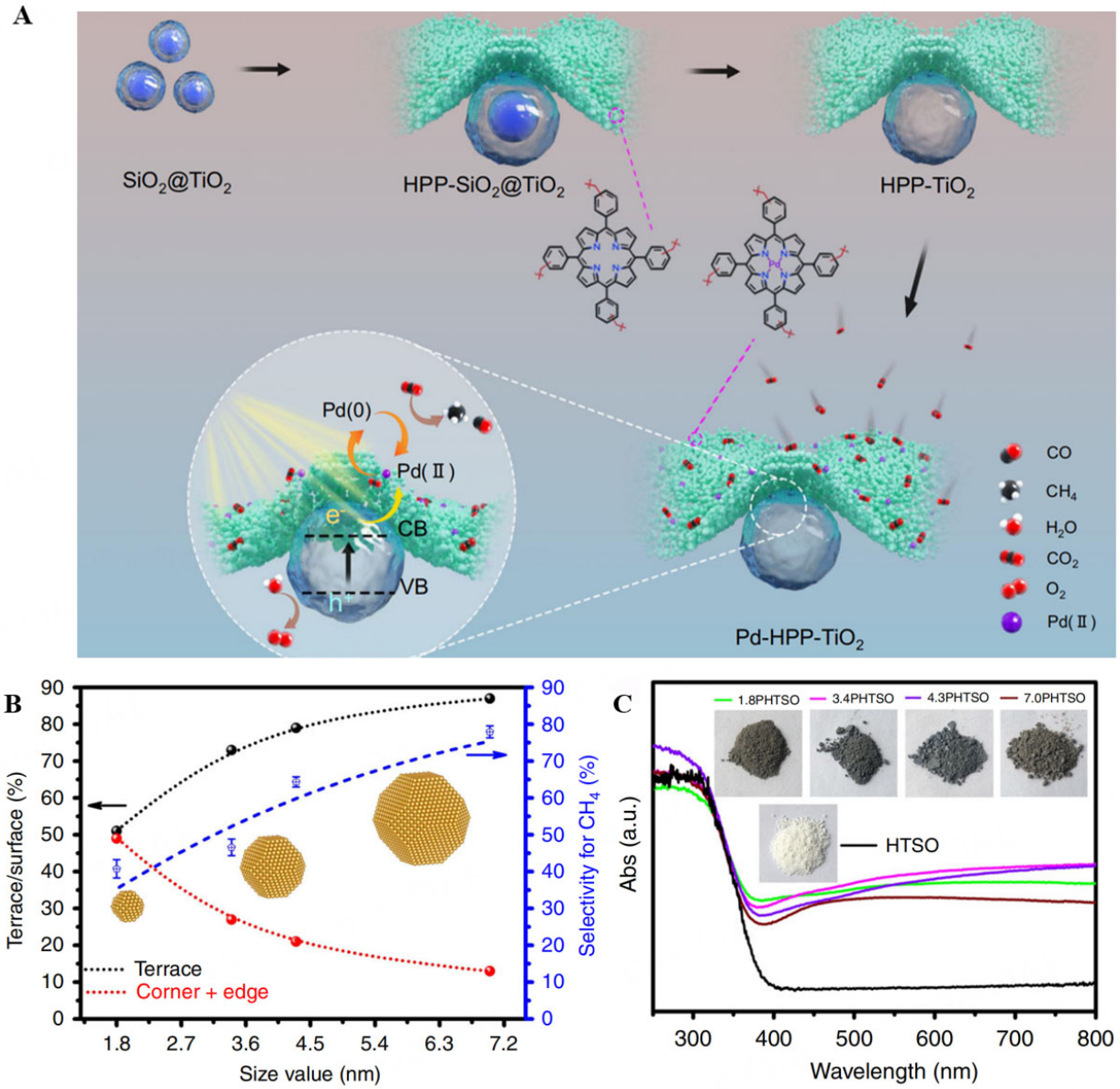

Figure 10. (A) Synthesis of porous Pd-HPP-TiO_2 and the possible mechanism of photocatalytic CO_2 reduction. Reprinted from Ref.[84] under the CC BY 4.0 license. (B) Correlations between the selectivity for CH_4 and surface site proportion as functions of the size of Pt NPs in xPHTSO (x = 1.8, 3.4, 4.3, and 7.0). (C) UV-Vis DRS spectra and the corresponding samples' photos (inset). Figure 10B and C is reprinted from Ref.[160] under the CC BY 4.0 license. HPP: Hyper-crosslinked porphyrin-based polymer; CB: conduction band; VB: valence band; PHTSO: Pt-loaded hollow TiO_2 with a silica overlayer; NP: nanoparticle; UV-Vis: ultraviolet-visible; DRS: diffuse reflectance spectroscopy.

Crucially, the catalytic efficacy of these metallic sinks is exquisitely sensitive to their geometric dimensions [Figure 10B and C]. Downsizing nanoparticles maximizes the population of low-coordinated surface atoms (corner and edge sites), augmenting electron trapping efficiency[160]. However, this miniaturization simultaneously alters the binding energetics of crucial intermediates, occasionally compromising target product selectivity. Conversely, larger nanoparticles predominantly expose terrace sites that thermodynamically favor specific multistep pathways, such as deep reduction to CH_4. This intricate trade-off dictates that metal cocatalyst design must transcend mere work-function matching, necessitating precise geometric tailoring to harmonize charge extraction kinetics with surface reaction specificity.

Pushing this geometric limit to the atomic scale, single-atom catalysts (SACs), such as Cu, Ni, and Co, have emerged as a transformative frontier. Unlike their nanoparticulate counterparts, SACs offer maximum atom

utilization, well-defined coordination environments, and the ability to modulate local electronic structures without fundamentally perturbing the host semiconductor's band architecture[161]. In model systems like Ag-anchored TiO_2, isolated Ag atoms operate as exclusive electron-trapping loci, substantially extending carrier lifetimes while stabilizing critical C_1 intermediates. The adjacent Ti sites synergistically facilitate water oxidation and proton supply, dictating a highly selective CO_2-to-CH_4 conversion pathway[101]. Similarly, anchoring isolated Cu species on polymeric carbon nitride (Cu-PCN) directly mediates electron transfer to adsorbed CO_2. Theoretical and *in situ* spectroscopic investigations corroborate that these atomic Cu sites significantly lower the activation barrier for *COOH formation, the rate-determining step, thereby steering the reaction with near-unity selectivity toward CO[151-153].

Complementing metallic systems, non-metallic and quasi-metallic cocatalysts leverage extended π-conjugated networks and high carrier mobilities to orchestrate directional charge routing. Carbon quantum dots (CQDs), acting as dynamic "electron reservoirs", provide rapid, delocalized electron transport channels that decisively mitigate bulk recombination when integrated into heterostructures (e.g., TiO_2/$SrTiO_3$ or Z-scheme $Bi_{12}O_{17}Cl_2$/NiAl-LDH)[162,163]. Furthermore, covalent organic frameworks (COFs) and conjugated polymers offer unprecedented molecular-level tunability. By constructing continuous interfacial π-electron channels, these materials expedite carrier migration while circumventing the strong, often irreversible metal-intermediate bonds characteristic of inorganic systems[164]. Consequently, non-metal cocatalysts typically govern intermediate stabilization via soft non-covalent interactions (e.g., π-π or electrostatic forces). By fine-tuning the adsorption energetics of species like *CO, these networks strategically suppress over-hydrogenation pathways, favoring highly selective CO evolution[165].

Table 4 systematically compiles recent benchmarks in cocatalyst-engineered photocatalysts, detailing the interplay between cocatalyst identity, half-reaction dynamics, and product distribution. Collectively, these studies underscore that rational cocatalyst integration is not merely a strategy to accelerate redox kinetics, but a fundamental prerequisite for bridging spatial charge extraction with precisely tailored interfacial reaction pathways in advanced CO_2 reduction systems.

Microstructure design

Microstructure engineering represents a quintessential strategy in photocatalytic CO_2 reduction (PCR) systems to fundamentally optimize mass diffusion and truncate charge transfer pathways. Dimensionality reduction to the 2D ultrathin limit effectively circumvents bulk recombination by ensuring that structural thicknesses are comparable to, or smaller than, the carrier diffusion length. For instance, atomic-scale $Bi_4O_5Br_2$ nanosheets exhibit drastically enhanced CO_2-to-CO activity compared to their bulk counterparts, as photogenerated electron-hole pairs are inherently forced to migrate toward surface active sites[186].

Furthermore, assembling 2D/2D heterojunctions (e.g., LDHs/MoS_2 or MXene/g-C_3N_4) maximizes interfacial contact area while minimizing transport resistance. In such architectures, highly conductive substrates such as MXenes function as robust "electron highways" expediting the directional funneling of photogenerated electrons to surface catalytic loci and markedly suppressing recombination[187,188].

Transitioning to 3D hierarchical designs, core-shell architectures introduce radial charge partitioning and coaxial transport cascades. By spatially decoupling oxidation and reduction half-reactions across a distinct geometric boundary, these structures foster robust built-in electric fields that orchestrate directional charge flow. Complex configurations, such as TiO_2@NiAl-LDH, Cu_2O@Cu-MOF, and ternary Cu_2O@NiAl-LDH/CQDs systems, vividly demonstrate how rational shell selection concentrates CO_2 molecules at the outermost reactive sites while spatially isolating them from internal charge generation centers, thereby firmly averting reverse charge recombination and enhancing multi-electron C_2 product selectivity[185,189-191].

Table 4. Summary of cocatalyst-modified photocatalysts for CO_2 reduction

Material	Vacancy type	Main product	Light sources	Sacrificial agents	AQE (%)	Rate μmol·g^{-1}·h^{-1}	Ref.
Co-Bi_3O_4Br	single-atom Co	CO	300 W Xe lamp	H_2O	-	107.1	[157]
Co-TCPP/Bi_3O_4Br	molecular Co	CO	300 W Xe lamp	H_2O	0.53 (380 nm)	71.3	[166]
CO_2N/BiOBr	non-noble nitride	CO	300 W Xe lamp	H_2O	-	67.8	[167]
Ni SAs-Bi_3O_4Br	single-atom Ni	HCOOH	300 W Xe lamp	H_2O	-	3632.6	[168]
$Cs_3Bi_2Br_9$/Co-NG	Co single-atom modified graphene	CO	300 W Xe lamp	H_2O	-	123.16	[169]
LaNi-Phen/COF-5	La-Ni bimetallic	CO	500 W Xe lamp	H_2O	-	605.8	[170]
Cu-HCOF	atomically dispersed Cu	CO	400-W high-pressure Hg lamp	TEOA	-	960	[171]
AgCo/Al-$SrTiO_3$	dual Ag/Co	CO	400-W high-pressure Hg lamp	H_2O	0.03 (365 nm)	105.4	[172]
Ag@Cr/Ga_2O_3	Ag-Cr core-shell	CO	300 W Xe lamp	H_2O	-	999.2	[173]
Cu/TiO_2	Cu	CH_4	300 W Xe lamp	H_2O	-	12.52	[174]
PtCuCN	Pt-loaded CuPc/g-C3N4	CH_4	LED light source (365 ± 10 nm)	TEOA	-	39.8	[51]
Pt-Au/R-TNTs	Pt-Au	CH_4	UV light irradiation (300 nm < λ < 400 nm)	H_2O	17.9 (365 nm)	360	[175]
Pt/TiO_2	Pt	CH_4	300 W Xe lamp λ ≥ 400 nm	H_2O	-	4.6	[176]
Pd TP/Pd SA-CN	Pd single atoms + twinned Pd nanoparticles	CO	600 mW/cm^2	H_2O	-	46.5	[177]
Pd NPs/TiO_2	Pd	CH_4	350 W Xe lamp	H_2O	-	28.5	[178]
g-C_3N_4/MoS_2/Cu	Cu	CO	300 W Xe lamp	H2O	3.2 (420 nm)	146.7	[179]
Co_1In_1/CN	Co-In dual single-atom	CH_4	UV light	H_2O	-	18.8	[180]
Pt@CeO_2/3D CN	Pt	CO	300 W Xe lamp	TEOA	-	4.69	[181]
$Cu_{0.7}Au_{0.3}$/TiO_2	Cu-Au bimetal	CO	300 W Xe lamp	H_2O	-	6.08	[182]
Ag-Cu/TiO_2	Ag-Cu dual	CO	300 W Xe lamp	H_2O	-	286.7	[183]
Au_6Ag_4/TiO_2	Au-Ag alloy	CO	300 W Xe lamp 320 nm < λ < 780 nm	H_2O	0.91 (450 nm)	99.54	[184]
Cu_2O@Cu-MOF/TiO_2	Cu_2O/Cu-MOF core-shell	CH_4	300 W Xe lamp	H_2O	-	366	[185]

AQE: Apparent quantum efficiency; TCPP: tetrakis(4-carboxyphenyl)porphyrin; SA: single-atom; TEOA: triethanolamine; R-TNT: Reduced TiO_2 nanotubes; MOF: metal-organic framework; NP: nanoparticle.

Porous and hollow microstructures culminate this spatial optimization by synchronously addressing the "light-harvesting, mass-transfer, and charge-separation" trifecta. As systematically elucidated in Figure 11, the advantages of these geometries are multidimensional. Internally, multi-shelled or hollow cavities induce severe light scattering and multireflection [Figure 11A], drastically amplifying the photon absorption path length. Electronically, the attenuated physical distance from the bulk to the solid-gas interface expedites charge extraction, a phenomenon universally corroborated by quenched steady-state photoluminescence (PL) [Figure 11B] and prolonged carrier lifetimes in time-resolved PL (TRPL) spectra [Figure 11C]. Concurrently, the interconnected porous networks massively expand surface accessibility, translating to superior CO_2 adsorption capacities [Figure 11D][194].

These synergistic mechanisms dictate the exceptional performance of practical systems, such as hierarchical porous $ZnIn_2S_4$ nested heterojunctions, hollow g-C_3N_4@TiO_2 microspheres, and hollow CeO_2 structures[193-196]. In these configurations, the structural voids not only host enriched active sites but

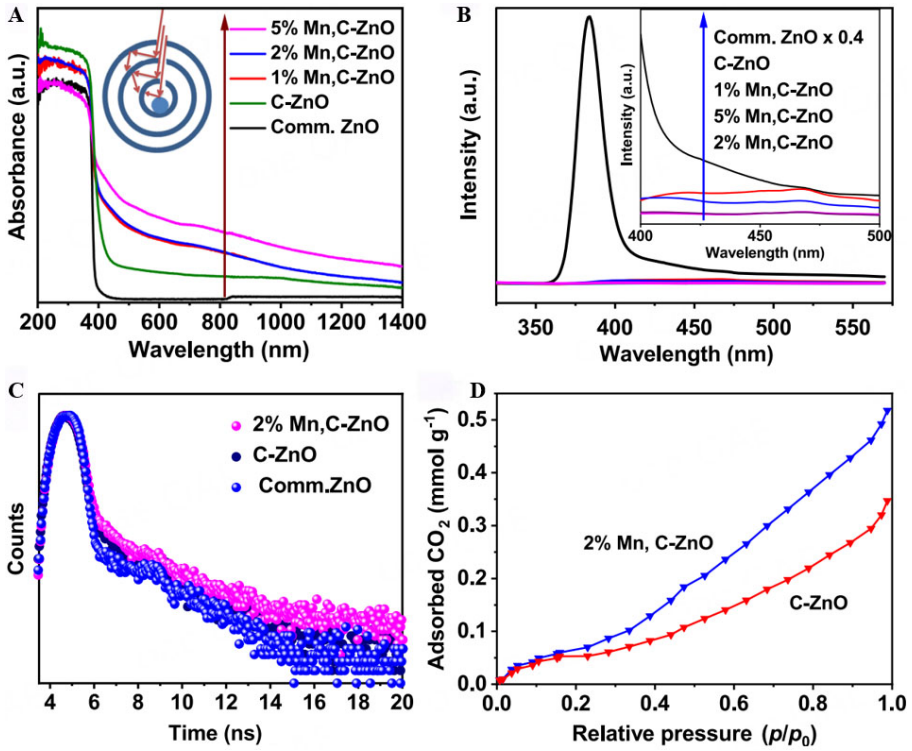

Figure 11. (A) UV-vis light absorption of the prepared photocatalysts and the inset represents the multiple reflection effect of the incident light inside the hollow cavities. (B) PL spectra of photocatalysts at excitation wavelength of 380 nm. (C) TRPL spectra of the samples. (D) CO_2 adsorption isotherm of C-ZnO CTSHSs and 2% Mn, C-ZnO-CTSHS samples. Figure 11 A-D is reprinted from Ref.[192] under the CC BY 4.0 license. UV-vis: Ultraviolet–visible; PL: photoluminescence; TRPL: time-resolved photoluminescence; CTSHS: core-triple shell hollow sphere.

fundamentally accelerate interfacial reaction kinetics under visible-light irradiation.

Table 5 summarizes state-of-the-art microstructure-engineered photocatalysts. Collectively, these geometric modulations, ranging from atomic 2D exfoliation to hierarchical 3D hollowing, demonstrate that macroscopic catalytic enhancements are inextricably linked to the precise nanoscale management of photon flux, reactant diffusion, and carrier transport vectors.

While the aforementioned strategies ranging from band engineering to microstructural design have individually propelled photocatalytic CO_2 reduction (PCR) forward, a critical appraisal reveals a persistent "single-strategy bottleneck". For instance, Z- and S-scheme heterojunctions elegantly preserve high-energy charge carriers, yet their efficacy is strictly tethered to interfacial electronic coupling; poorly matched work functions or structural deviations inevitably spawn parasitic recombination pathways. Similarly, while metallic sinks and Schottky junctions expedite charge extraction, their optimization is plagued by a delicate balancing act, as excessive loading invariably triggers light-shielding effects or active-site occlusion. Furthermore, morphological tuning and defect engineering (e.g., oxygen vacancies) effectively shorten diffusion lengths and enhance reactant adsorption, respectively, but they often lack the intrinsic thermodynamic driving force required to independently orchestrate long-distance, directional charge separation.

Consequently, tackling the PCR bottleneck demands a paradigm shift from isolated component optimization to the synergistic integration of multi-dimensional strategies. This synergy transcends a mere mathematical superposition of effects; rather, it orchestrates a holistic reconstruction of charge-transfer networks across

Table 5. Summary of microstructure-engineered photocatalysts for CO_2 reduction

Material	Vacancy type	Main product	Light sources	Sacrificial agents	AQE (%)	Rate μmol·g^{-1}·h^{-1}	Ref.
$Bi_4O_5Br_2$-UN	2D nanosheets	CO	300 W Xe lamp	H_2O	-	31.57	[186]
TC/g-C_3N_4	2D/2D heterojunction	CO	300 W Xe lamp λ ≥ 420 nm	H_2O	-	5.19	[188]
TiO_2@CN	core-shell Z-scheme	CO	300 W Xe lamp 320 nm < λ < 780 nm	H_2O	1.829 (400 nm)	26.89	[191]
Cu_2O@NA-LDH/CQDs	ternary core-shell	C_2H_6	300 W Xe lamp λ ≥ 420 nm	TEOA	-	8.18	[190]
NiAl-LDH@TiO_2/Ti_3C_2	hierarchical core-shell	CO	300 W Xe lamp	H_2O	0.81 (365 nm)	86.52	[197]
CNGA/CdS	ultrathin porous nanosheets	CO	300 W Xe lamp λ ≥ 420 nm	H_2O	0.65 (500 nm)	32.75	[198]
CDs-1/CdS	hierarchical hollow microspheres	CO	300 W Xe lamp	TEOA	-	16.09	[199]
H-$Cs_3Sb_2Br_9$	hollow nanospheres	CO	300 W Xe lamp λ ≥ 400 nm	CH_3OH	2.65 (400 nm)	1876.3	[200]
$Bi_4O_5Br_2$	hollow core-shell	CO	300 W Xe lamp	H_2O	-	3.61	[201]
$NiCO_2V_2O_8$	hollow nanospheres	CO	300 W Xe lamp λ ≥ 420 nm	TEOA	5.76 (380 nm)	198.65	[202]
g-C_3N_4/rGO/NiAl-LDHs	layered hierarchical heterojunction	CH_4	300 W Xe lamp	TEOA	1.36 (380 nm)	20	[203]
BWO	ultrathin nanosheets	CO	300 W Xe lamp	H_2O	0.35 (350 nm)	19.45	[204]
F-2D BMO	2D nanosheets	CO	300 W Xe lamp	H_2O	1.5 (420 nm)	5.6	[205]
CdS/TiO_2	hollow microspheres	CH_4	350 W Xe lamp	H_2O	-	27.85	[206]
Cu-HCOF	hollow COF structure	CO	500 W Xe lamp	TEOA	-	960	[171]
Bi-CuO	core-shell	CO	300 W Xe lamp	H_2O	-	106.07	[207]
Ag/hollow-TiO_2	hollow spheres	CH_4	300 W Xe lamp	H_2O	-	6.72	[208]
Pt/β-SiC HS	open-mouthed hollow spheres	CH_4	300 W Xe lamp	H_2O	-	16.8	[209]
Co_9S_8@$ZnIn_2S_4$/CdS	hollow core-shell nanoreactor	CO	300 W Xe lamp	H_2O	-	82.1	[210]
SnS_2/CeO_2	2D/0D heterojunction	CO	300 W Xe lamp	TEOA	-	16.27	[211]
$SiW_{11}Cu$@TiO_2	heterointerface core-shell-like composite	CO	300 W Xe lamp	TEOA	-	84.12	[212]
Au/CdS HMCHPs	hierarchical multi-cavity hollow particles	CO	300 W Xe lamp λ ≥ 400 nm	TEOA	0.61 (420 nm)	3,758	[213]
Ni/Bi-30	porous ultrathin nanosheets	CO	460 nm LED	TEOA	-	10.2	[214]
NFMS	2D/2D heterojunction	CO	300 W Xe lamp	H_2O	-	2.68	[187]

AQE: Apparent quantum efficiency; UN: ultrathin nanosheet; CNGA: glucose-assisted ultrathin porous nitrogen-vacancy carbon nitride nanosheet; CD: carbon dot; CQD: carbon quantum dot; LDH: layered double hydroxide; BMO: Bi_2MoO_6; BWO: Bi_2WO_6; HMCHP: hierarchical multi-Cavity hollow particle; NFMS: NiFe-LDH/MoS_2; COF: covalent organic framework; TEOA: triethanolamine; LED: light-emitting diode.

diverse spatiotemporal scales. For example, coupling defect engineering with built-in electric fields, as demonstrated in oxygen-vacancy-rich $Ni_2P_2O_7$/g-C_3N_4 heterojunctions[215] or ferroelectric Bi_3TiNbO_9 nanosheets[216], establishes a powerful dual-regulation mechanism. In these systems, vacancies serve as localized reactant-trapping and activation loci, while the overarching internal polarization fields forcefully dictate directional carrier migration, synchronously suppressing bulk recombination and accelerating surface reaction kinetics.

Furthermore, integrating Schottky junctions with plasmonic architectures introduces distinct energetic advantages. In plasmonic Ag/TiO_2 systems, the localized surface plasmon resonance (LSPR) effect harvests lower-energy photons to inject hot electrons, while the proximal Schottky barrier immediately rectifies their flow, preventing back-transfer. Time-resolved spectroscopy confirms that this precise energetic and spatial synchronization profoundly amplifies overall multi-electron transfer efficiency[217].

Ultimately, the zenith of photocatalytic CO_2 reduction will not be reached through isolated structural tweaks, but through the mastery of multi-level coupled mechanisms. By hierarchically integrating interfacial electric fields, precise defect distributions, and optimally configured active sites, researchers can construct continuous, energetically cascaded electron "highways" from bulk generation centers directly to adsorbed CO_2 molecules. This synergy-driven design paradigm stands as the definitive roadmap for circumventing intrinsic thermodynamic limitations and steering PCR technology toward viable practical applications.

CONCLUSIONS AND OUTLOOK

This review systematically discusses the charge separation process in photocatalytic CO_2 reduction (PCR) systems from a multi-scale perspective, integrating bulk generation, interfacial migration, and surface reaction coupling within a unified framework. As emphasized throughout the manuscript, charge separation efficiency is the core bottleneck governing PCR performance, as it directly determines the effective utilization of photogenerated carriers in multi-electron CO_2 conversion processes.

By correlating thermodynamic driving forces with kinetic competition, we clarify that charge separation is not an isolated step but a dynamic process governed by the interplay between carrier generation, migration, and recombination across different spatial scales. Intrinsic limitations such as bulk recombination, interfacial energy mismatch, and surface charge consumption inefficiency, together with non-intrinsic factors including light harvesting and CO_2 activation barriers, collectively define the upper limit of photocatalytic efficiency.

From a materials design perspective, we further summarize that charge separation regulation must rely on synergistic strategies rather than single-factor optimization. In particular, heterojunction engineering, including type-II, Z-scheme, S-scheme, and Schottky junctions, provides effective pathways for directional charge transfer and redox potential preservation. Among these, Z-scheme and S-scheme systems are especially effective in balancing charge separation with strong redox capability, while Schottky junctions offer an additional route for surface electron extraction and reaction-site coupling.

In addition, as highlighted in the characterization section, reliable evaluation of charge separation requires a multi-technique and multi-timescale approach. No single method can fully describe the complete carrier evolution process; instead, only the convergence of spectroscopic, electrochemical, ultrafast kinetic, and operando techniques can reconstruct the full pathway from photogeneration to catalytic consumption. Overall, this work establishes a unified picture linking charge generation, separation, transport, and utilization in PCR systems, providing mechanistic guidance for the rational design of high-efficiency photocatalysts.

Despite the remarkable progress in regulating charge separation for photocatalytic CO_2 reduction (PCR), several critical challenges remain before translating these advances into practical applications. Future research should move beyond isolated optimization strategies toward data-driven, mechanism-oriented, and application-relevant catalyst design frameworks, with particular emphasis on charge behavior under realistic reaction environments.

First, AI-assisted catalyst design is expected to play a transformative role in accelerating the discovery of high-performance PCR systems. Machine learning has been widely recognized as an effective tool for accelerating molecular and materials discovery, and its application in electrocatalyst and photocatalyst design has provided new opportunities for identifying structure-property-activity relationships[218,219]. By integrating machine learning with density functional theory calculations and high-throughput experimentation, it becomes possible to establish quantitative correlations between electronic structure descriptors, such as band alignment, charge density distribution, carrier lifetime, and catalytic performance. In particular, AI models can be trained to predict charge separation efficiency, interfacial charge-transfer kinetics, and optimal heterojunction configurations, thereby guiding the rational design of multi-component catalysts beyond empirical trial-and-error approaches.

Second, the development of advanced operando characterization techniques is essential to directly probe charge behavior under working conditions. Although PL, TRPL, EIS, and TAS provide valuable information on carrier recombination and transport, they often cannot fully capture real-time charge redistribution during CO_2 adsorption, activation, and conversion. Emerging *in situ*/operando spectroscopies, including operando XPS, XAS, FT-IR/DRIFTS, Raman, and EPR, can provide more direct evidence for photoinduced charge migration, interfacial band bending, active-site evolution, and reaction intermediate formation under illumination[220]. Therefore, future studies should combine ultrafast spectroscopy, operando electronic-structure characterization, and theoretical calculations to reconstruct the full charge evolution pathway from photogeneration to surface reaction.

Third, the rational design of multi-strategy synergistic catalysts should be significantly strengthened. Instead of relying on a single modulation strategy, future PCR catalysts should integrate heterojunction engineering, defect regulation, cocatalyst loading, morphology optimization, and internal electric-field construction into unified architectures. In such systems, charge separation is not governed by one isolated interface but by multi-level coupling across the bulk, interface, and surface. For example, ferroelectric polarization coupled with oxygen vacancies can simultaneously promote bulk charge separation and surface CO_2 activation[220], while plasmonic metal/semiconductor interfaces can couple Schottky-barrier-driven charge extraction with hot-electron injection and enhanced light absorption. These examples indicate that synergistic catalyst design should aim to regulate the entire charge-transfer network, including carrier generation, directional migration, interfacial accumulation, and final utilization at CO_2 reduction sites.

Fourth, a deeper understanding of charge separation mechanisms under conditions closer to practical application is urgently needed. Most current PCR studies are still performed under idealized conditions, such as high-purity CO_2, sacrificial agents, static batch reactors, and simplified gas-solid or liquid-solid interfaces. However, under realistic conditions, including low-concentration CO_2, fluctuating light intensity, water vapor, gas-liquid-solid interfaces, and continuous-flow operation, charge behavior may be strongly affected by mass transfer, competitive adsorption, surface reconstruction, and local reaction microenvironments[221,222]. Therefore, future research should investigate charge transport, recombination, and interfacial electron utilization in diluted CO_2 systems and continuous-flow photoreactors. Such studies will be essential for bridging the gap between laboratory-scale photocatalytic activity and scalable CO_2 conversion systems.

Finally, from a fundamental perspective, future research should aim to establish a unified theoretical framework for charge behavior that integrates thermodynamics, kinetics, and interfacial physics. This framework should quantify the competition between charge transfer and recombination across multiple spatial and temporal scales and identify key descriptors governing charge separation efficiency. In summary, advancing photocatalytic CO_2 reduction toward practical implementation requires a paradigm shift from

material-centered optimization to charge-behavior-centered design, supported by AI-driven catalyst discovery, operando characterization, multi-strategy synergistic engineering, and realistic-condition mechanism studies. These directions will provide new opportunities for developing highly efficient, selective, stable, and scalable photocatalytic CO_2 reduction systems.

DECLARATIONS

Authors' contributions

Writing - review & editing: Wang, J.; Wang, C.
Review: Fan, C.; Liu, H.
Funding acquisition: Wang, J.
Supervision: Wang, J.; Cheng, J.; Yang, H. Y.

Availability of data and materials

Not applicable.

AI and AI-assisted tools statement

During the preparation of this manuscript, the AI tool ChatGPT (version 5.5, released 2026-04-24) was used solely for language editing. The tool did not influence the study design, data collection, analysis, interpretation, or the scientific content of the work. All authors take full responsibility for the accuracy, integrity, and final content of the manuscript.

Financial support and sponsorship

This work was supported by the National Natural Science Foundation of China (No. 52372151).

Conflicts of interest

Hui Ying Yang is an Associate Editor of the journal *Energy Z*; however, she had no involvement in the editorial handling of this manuscript, including the selection of reviewers, manuscript processing, or decision-making. The other authors declare that they have no conflicts of interest.

Ethical approval and consent to participate

Not applicable.

Consent for publication

Not applicable.

REFERENCES

1. Akbar, H.; Javed, M. S.; Iqbal, S. T.; et al. A review of photocatalytic CO_2 reduction: exploring sustainable carbon emission mitigation from thermodynamics to kinetics and strategies for enhanced efficiency. *J. Korean. Ceram. Soc.* **2024**, *61*, 367-90. DOI
2. Wang, L.; Zhu, B.; Zhang, J.; Ghasemi, J. B.; Mousavi, M.; Yu, J. S-scheme heterojunction photocatalysts for CO_2 reduction. *Matter* **2022**, *5*, 4187-211. DOI
3. Fang, S.; Rahaman, M.; Bharti, J.; et al. Photocatalytic CO_2 reduction. *Nat. Rev. Methods. Primers.* **2023**, *3*, 243. DOI
4. Fu, C.; Wan, Z.; Yang, X.; Zhang, J.; Zhang, Z. Artificial CO_2 photoreduction: a review of photocatalyst design and product selectivity regulation. *J. Mater. Chem. A.* **2024**, *12*, 28618-57. DOI
5. Long, D.; Li, J.; Qian, G.; et al. Photocatalytic reduction of low-concentration CO_2: progress and challenges. *Coord. Chem. Rev.* **2026**, *549*, 217246. DOI
6. Choi, S. H.; Song, I.; Dong, W. J. Recent progress of photothermal catalysts for carbon dioxide conversion. *Energy. Mater.* **2025**, *5*, 500062. DOI
7. Zhang, J.; Jiang, J.; Lei, Y.; et al. Photocatalytic CO_2 reduction reaction: Influencing factors, reaction pathways and dominant catalysts. *Sep. Purif. Technol.* **2024**, *328*, 125056. DOI

8. Wang, Z.; Xiang, F.; Chen, C.; Wang, Y.; Zhao, X.; Fan, W. Boosting photocatalytic reduction of low-concentration CO_2 to CO via hydrophilic/CO_2-philic interface microenvironment engineering in Ag/TiO_{2-x} Schottky junctions. *Appl. Catal. B:. Environ. Energy.* **2026**, *381*, 125906. DOI
9. Sun, B.; Mo, J.; Wang, Q.; et al. Outstanding specific yield strength of a refractory high-entropy composite at an ultrahigh temperature of 2273 K. *J. Mater. Sci. Technol.* **2023**, *166*, 145-54. DOI
10. Li, X.; Yu, J.; Jaroniec, M.; Chen, X. Cocatalysts for selective photoreduction of CO_2 into solar fuels. *Chem. Rev.* **2019**, *119*, 3962-4179. DOI
11. Park, Y. H.; Murali, G.; Modigunta, J. K. R.; In, I.; In, S. I. Recent advances in quantum dots for photocatalytic CO_2 reduction: a mini-review. *Front. Chem.* **2021**, *9*, 734108. DOI PubMed PMC
12. Jiang, C.; Moniz, S. J. A.; Wang, A.; Zhang, T.; Tang, J. Photoelectrochemical devices for solar water splitting - materials and challenges. *Chem. Soc. Rev.* **2017**, *46*, 4645-60. DOI PubMed
13. Li, Y.; Bian, Y.; Qin, H.; Zhang, Y.; Bian, Z. Photocatalytic reduction behavior of hexavalent chromium on hydroxyl modified titanium dioxide. *Appl. Catal. B. Environ.* **2017**, *206*, 293-9. DOI
14. Wang, J.; Sun, Y.; Lai, J.; et al. Two-dimensional graphitic carbon nitride/N-doped carbon with a direct Z-scheme heterojunction for photocatalytic generation of hydrogen. *Nanoscale. Adv.* **2021**, *3*, 6580-6. DOI PubMed PMC
15. Xu, Q.; Zhang, L.; Cheng, B.; Fan, J.; Yu, J. S-scheme heterojunction photocatalyst. *Chem* **2020**, *6*, 1543-59. DOI
16. Eshete, M.; Li, X.; Yang, L.; et al. Charge steering in heterojunction photocatalysis: general principles, design, construction, and challenges. *Small. Sci.* **2023**, *3*, 2200041. DOI PubMed PMC
17. Kovačič, Ž.; Likozar, B.; Huš, M. Photocatalytic CO_2 reduction: a review of *ab initio* mechanism, kinetics, and multiscale modeling simulations. *ACS. Catal.* **2020**, *10*, 14984-5007. DOI
18. Thompson, W. A.; Sanchez, Fernandez. E.; Maroto-Valer, M. M. Review and analysis of CO_2 photoreduction kinetics. *ACS. Sustainable. Chem. Eng.* **2020**, *8*, 4677-92. DOI
19. Ma, J.; Miao, T. J.; Tang, J. Charge carrier dynamics and reaction intermediates in heterogeneous photocatalysis by time-resolved spectroscopies. *Chem. Soc. Rev.* **2022**, *51*, 5777-94. DOI PubMed
20. Makuła, P.; Pacia, M.; Macyk, W. How to correctly determine the band gap energy of modified semiconductor photocatalysts based on UV-vis spectra. *J. Phys. Chem. Lett.* **2018**, *9*, 6814-7. DOI PubMed
21. Miao, T. J.; Tang, J. Characterization of charge carrier behavior in photocatalysis using transient absorption spectroscopy. *J. Chem. Phys.* **2020**, *152*, 194201. DOI PubMed
22. Kirchartz, T.; Márquez, J. A.; Stolterfoht, M.; Unold, T. Photoluminescence-based characterization of halide perovskites for photovoltaics. *Adv. Energy. Mater.* **2020**, *10*, 1904134. DOI
23. He, B.; Zhang, C.; Luo, P.; Li, Y.; Lu, T. Integrating Z-scheme heterojunction of Co_1-C_3N_4@α-Fe_2O_3 for efficient visible-light-driven photocatalytic CO_2 reduction. *Green. Chem.* **2020**, *22*, 7552-9. DOI
24. De, Pasquale. L.; Tavella, F.; Longo, V.; et al. The role of substrate surface geometry in the photo-electrochemical behaviour of supported TiO_2 nanotube arrays: a study using electrochemical impedance spectroscopy (EIS). *Molecules* **2023**, *28*, 3378. DOI PubMed PMC
25. Kumar, S.; Ojha, K.; Ganguli, A. K. Interfacial charge transfer in photoelectrochemical processes. *Adv. Materials. Inter.* **2017**, *4*, 1600981. DOI
26. Wang, K.; Cheng, Q.; Hou, W.; et al. Unlocking the charge-migration mechanism in S-scheme junction for photoreduction of diluted CO_2 with high selectivity. *Adv. Funct. Materials.* **2024**, *34*, 2309603. DOI
27. Zhang, J.; Zhang, L.; Wang, W.; Yu, J. *In situ* irradiated X-ray photoelectron spectroscopy investigation on electron transfer mechanism in s-scheme photocatalyst. *J. Phys. Chem. Lett.* **2022**, *13*, 8462-9. DOI
28. Wang, L.; Cheng, B.; Zhang, L.; Yu, J. *In situ* irradiated XPS investigation on S-scheme TiO_2@$ZnIn_2S_4$ photocatalyst for efficient photocatalytic CO_2 reduction. *Small* **2021**, *17*, e2103447. DOI
29. Yang, J.; Wang, J.; Wang, G.; Wang, K.; Li, J.; Zhao, L. In situ irradiated XPS investigation on S-scheme TiO_2/Bi_2S_3 photocatalyst with high interfacial charge separation for highly efficient photothermal catalytic CO_2 reduction. *J. Mater. Sci. Technol.* **2024**, *189*, 86-95. DOI
30. Chen, R.; Zhu, J.; An, H.; Fan, F.; Li, C. Unravelling charge separation via surface built-in electric fields within single particulate photocatalysts. *Faraday. Discuss.* **2017**, *198*, 473-9. DOI
31. Kondo, A.; Yin, G.; Srinivasan, N.; Atarashi, D.; Sakai, E.; Miyauchi, M. Kelvin probe imaging of photo-injected electrons in metal oxide nanosheets from metal sulfide quantum dots under remote photochromic coloration. *Nanoscale* **2015**, *7*, 12510-5. DOI PubMed

32. Kasimayan, U.; Nadarajan, A.; Singaravelu, C. M.; et al. *In-situ* DRIFT investigation of photocatalytic reduction and oxidation properties of SiO_2@α-Fe_2O_3 core-shell decorated RGO nanocomposite. *Sci. Rep.* **2020**, *10*, 2128. DOI PubMed PMC
33. Cui, J.; Shen, Z.; Cao, G.; Zhao, X.; Li, W. Highly efficient and 100 % selectivity of CO generation via CO_2 photoreduction over a novel CsBr@$CuBr_2$ heterojunction. *Heliyon* **2024**, *10*, e33653. DOI PubMed PMC
34. Que, M.; Cai, W.; Chen, J.; Zhu, L.; Yang, Y. Recent advances in g-C_3N_4 composites within four types of heterojunctions for photocatalytic CO_2 reduction. *Nanoscale* **2021**, *13*, 6692-712. DOI
35. Zhang, G.; Wang, Z.; Wu, J. Construction of a Z-scheme heterojunction for high-efficiency visible-light-driven photocatalytic CO_2 reduction. *Nanoscale* **2021**, *13*, 4359-89. DOI
36. Ng, B. J.; Putri, L. K.; Kong, X. Y.; Teh, Y. W.; Pasbakhsh, P.; Chai, S. P. Z-scheme photocatalytic systems for solar water splitting. *Adv. Sci. (Weinh).* **2020**, *7*, 1903171. DOI PubMed PMC
37. Xu, Q.; Zhang, L.; Yu, J.; Wageh, S.; Al-Ghamdi, A. A.; Jaroniec, M. Direct Z-scheme photocatalysts: principles, synthesis, and applications. *Mater. Today.* **2018**, *21*, 1042-63. DOI
38. Liao, G.; Li, C.; Liu, S.; Fang, B.; Yang, H. Z-scheme systems: from fundamental principles to characterization, synthesis, and photocatalytic fuel-conversion applications. *Phys. Rep.* **2022**, *983*, 1-41. DOI
39. Chen, X.; Zhao, C.; Wu, H.; Shi, Y.; Chen, C.; Zhou, X. Two-dimensional ZnS/SnS_2 heterojunction as a direct Z-scheme photocatalyst for overall water splitting: a DFT study. *Materials. (Basel).* **2022**, *15*, 3786. DOI PubMed PMC
40. Wang, X.; Wang, X.; Huang, J.; Li, S.; Meng, A.; Li, Z. Interfacial chemical bond and internal electric field modulated Z-scheme S_v-$ZnIn_2S_4$/$MoSe_2$ photocatalyst for efficient hydrogen evolution. *Nat. Commun.* **2021**, *12*, 4112. DOI PubMed PMC
41. Wang, Y.; Shang, X.; Shen, J.; et al. Direct and indirect Z-scheme heterostructure-coupled photosystem enabling cooperation of CO_2 reduction and H_2O oxidation. *Nat. Commun.* **2020**, *11*, 3043. DOI PubMed PMC
42. Feng, B.; Wang, Q.; Liu, P.; et al. Z-scheme heterojunction enhanced photocatalytic performance for CO_2 reduction to CH_4. *Nanoscale* 2024;16:17616-23.[DOI:10.1039/d4nr02897j] Caution!.
43. Pan, M.; Zheng, L.; Cai, C.; Wang, W. Z-Scheme ZnO/$ZnAl_2O_4$ heterojunction with synergistic effects for enhanced photocatalytic CO_2 reduction. *Molecules* **2025**, *30*, 2626. DOI PubMed PMC
44. Xue, Y.; Wei, K.; Yang, J.; et al. Z-scheme heterojunction between CuS and PCN-222 for efficient photothermal catalytic CO_2 reduction. *Mol. Catal.* **2025**, *587*, 115511. DOI
45. Zhao, J.; Ji, M.; Chen, H.; et al. Interfacial chemical bond modulated $Bi_{19}S_{27}Br_3$/g-C_3N_4 Z-scheme heterojunction for enhanced photocatalytic CO_2 conversion. *Appl. Catal. B:. Environ. Energy.* **2022**, *307*, 121162. DOI
46. Li, J.; Wei, F.; Xiu, Z.; Han, X. Direct Z-scheme charge transfer of Bi_2WO_6/$InVO_4$ interface for efficient photocatalytic CO_2 reduction. *Chem. Eng. J.* **2022**, *446*, 137129. DOI
47. Zhang, Y.; Jiang, X.; Jiang, M.; Dong, W.; Zhao, J.; Li, D. Enhancing CO_2 photoreduction efficiency via direct Z-scheme CuS/NH_2-UiO-66 heterojunction with high selectivity of CO_2 to CO. *J. Solid. State. Chem.* **2025**, *348*, 125398. DOI
48. Wang, Y.; Cao, Y.; Wei, S.; et al. N-Bi covalently connected Z-scheme heterojunction by in situ anchoring BiOCl on triazine-based bromine-substituted covalent organic frameworks for the enhanced photocatalytic reduction of CO_2 and Cr (VI). *Chem. Eng. J.* **2025**, *505*, 159349. DOI
49. Zeng, X.; Zhu, J.; Xia, W.; et al. Ni-doped flower-like BiOCl/MXene composite catalysts for enhanced CO_2 reduction performance. *Ionics* **2025**, *31*, 11991-2003. DOI
50. Zhang, Y.; Nwaji, N.; Wu, L.; et al. $MAPbBr_3$/Bi_2WO_6 Z-scheme-heterojunction photocatalysts for photocatalytic CO_2 reduction. *J. Mater. Sci.* **2024**, *59*, 1498-512. DOI
51. Chen, J.; Lu, J.; Lang, R.; et al. Enhanced and selective photocatalytic reduction of CO_2 to CH_4 using a Pt-loaded CuPc/g-C_3N_4 Z-scheme heterojunction catalyst. *Green. Energy. Environ.* **2025**, *10*, 1348-58. DOI
52. Mehregan, S.; Hayati, F.; Mehregan, M.; et al. Exploring the visible light-assisted conversion of CO_2 into methane and methanol, using direct Z-scheme TiO_2@g-C_3N_4 nanosheets: synthesis and photocatalytic performance. *Environ. Sci. Pollut. Res. Int.* **2022**, *29*, 74951-66. DOI
53. Wang, T.; He, X.; Li, Y.; Li, J. Novel poly(piperazine-amide) (PA) nanofiltration membrane based poly(m-phenylene isophthalamide) (PMIA) hollow fiber substrate for treatment of dye solutions. *Chem. Eng. J.* **2018**, *351*, 1013-26. DOI
54. Li, M.; Cui, H.; Zhao, Y.; et al. S-scheme heterojunction photocatalysts for CO_2 reduction. *Catalysts* **2024**, *14*, 374. DOI
55. Zou, J.; Li, L.; Tan, N.; Zhang, K.; Wang, L.; Chen, Z. Construction of S-scheme heterojunction with interfacial chemical bonds for enhanced photocatalytic CO_2 reduction. *Appl. Surf. Sci.* **2026**, *719*, 165001. DOI

56. Wang, P.; Ba, X.; Zhang, X.; et al. Direct Z-scheme heterojunction of PCN-222/$CsPbBr_3$ for boosting photocatalytic CO_2 reduction to HCOOH. *Chem. Eng. J.* **2023**, *457*, 141248. DOI
57. Wang, F.; Zhang, S.; Jing, W.; Qiu, H.; Liu, Y.; Guo, L. Double Z-scheme in SnO_2/SnS_2/Cu_2SnS_3 heterojunction for photocatalytic reduction of CO_2 to ethanol. *J. Mater. Sci. Technol.* **2024**, *189*, 146-54. DOI
58. Xu, Y.; Yu, J.; Long, J.; Tu, L.; Dai, W.; Yang, L. Z-scheme heterojunction of SnS_2/Bi_2WO_6 for photoreduction of CO_2 to 100% alcohol products by promoting the separation of photogenerated charges. *Nanomaterials. (Basel).* **2022**, *12*, 2030. DOI PubMed PMC
59. Chen, Q.; Wang, S.; Miao, B.; Chen, Q. Dual p-n Z-scheme heterostructure boosted superior photoreduction CO_2 to CO, CH_4 and C_2H_4 in In_2S_3/MnO_2/BiOCl photocatalyst. *J. Colloid. Interface. Sci.* **2024**, *663*, 1005-18. DOI
60. Tian, Z. Y.; Kong, L. H.; Wang, Y.; et al. Construction of low-cost Z-scheme heterostructure Cu_2O/PCN for highly selective CO_2 photoreduction to methanol with water oxidation. *Small* **2021**, *17*, e2103558. DOI
61. Jiao, Q.; Gao, B.; Zhang, L.; et al. Rational design of a Z-scheme 2D/2D S-doped g-C_3N_4/Bi_2MoO_6 heterostructure for enhanced photocatalytic CO_2 reduction to CH_3OH. *Colloids. Surf. A. Physicochem. Eng. Asp.* **2025**, *726*, 137798. DOI
62. Wang, M.; Zeng, S.; Woldu, A. R.; Hu, L. $BiVO_4$/Bi_2S_3 Z-scheme heterojunction with MnO_x as a cocatalyst for efficient photocatalytic CO_2 conversion to methanol by pure water. *Nano. Energy.* **2022**, *104*, 107925. DOI
63. Xu, F.; Zhao, F.; Deng, X.; et al. Integrating S-scheme photocatalysis with tandem carbonylation: a green and scalable strategy for CO_2 valorization. *Nat. Commun.* **2025**, *16*, 6882. DOI PubMed PMC
64. Zhang, X.; Kim, D.; Yan, J.; Lee, L. Y. S. Photocatalytic CO_2 reduction enabled by interfacial S-scheme heterojunction between ultrasmall copper phosphosulfide and g-C_3N_4. *ACS. Appl. Mater. Interfaces.* **2021**, *13*, 9762-70. DOI
65. Wu, J.; Li, K.; Li, J.; et al. An S-scheme heterojunction constructed from α-Fe_2O_3 and In-doped carbon nitride for high-efficiency CO_2 photoreduction. *Catal. Sci. Technol.* **2022**, *12*, 1520-9. DOI
66. Jing, Y. N.; Yin XL. CuO/TiO_2 S-scheme heterostructure for efficient photocatalytic CO_2 reduction with nearly 100 % CO selectivity. *Ceram. Int.* **2025**, *51*, 8260-8. DOI
67. Wang, R.; Wang, Z.; Shang, X.; Yang, Y.; Ding, J.; Zhong, Q. A novel S-scheme heterojunction constructed by Ti-based hydrotalcite decorating MOFs for boosting CO_2-to-CO photoreduction and mechanism insights. *J. Mater. Chem. A.* **2023**, *11*, 630-41. DOI
68. Pei, L.; Luo, Z.; Zhong, J.; et al. Carbon dioxide photoreduction using a photocatalyst with prolonged charge-separated states and excess electron reservoirs. *Cell. Rep. Phys. Sci.* **2024**, *5*, 102194. DOI
69. Zhang, Y.; Xu, M.; Zhou, W.; et al. Fabricated ZnO@$ZnIn_2S_4$ S-scheme heterojunction photocatalyst for enhanced electron-transfer and CO_2 reduction. *J. Colloid. Interface. Sci.* **2023**, *650*, 1762-72. DOI
70. Wang, T.; Lu, J.; Chen, J.; Wang, C.; Li, K.; Mei, Y. Achieving high CH_4 selectivity in CO_2 photoreduction *via* S-type MoO_3/g-C_3N_4 heterojunction with Pt co-catalyst. *Catal. Sci. Technol.* **2025**, *15*, 2938-49. DOI
71. Ma, Q.; Ren, J.; Sun, X.; et al. Enhanced CO_2 photoreduction over S-scheme Sdoped-$BiVO_4$/AgCl heterostructures and interface interaction mediated selective generation of CH_4. *Chem. Eng. J.* **2025**, *509*, 161444. DOI
72. Yang, H.; Hou, H.; Yang, M.; et al. Engineering the S-scheme heterojunction between NiO microrods and MgAl-LDH nanoplates for efficient and selective photoreduction of CO_2 to CH_4. *Chem. Eng. J.* **2023**, *474*, 145813. DOI
73. Zhang, Z.; Liu, X.; Yuanling, L.; Yu, H.; Li, W.; Yu, H. Unveiling the role of Ag-Sb bimetallic S-scheme heterojunction for vis-NIR-light driven selective photoreduction CO_2 to CH_4. *Appl. Catal. B. Environ.* **2022**, *319*, 121960. DOI
74. Wang, K.; Feng, X.; Shangguan, Y.; Wu, X.; Chen, H. Selective CO_2 photoreduction to CH_4 mediated by dimension-matched 2D/2D Bi_3NbO_7/g-C_3N_4 S-scheme heterojunction. *Chin. J. Catal.* **2022**, *43*, 246-54. DOI
75. Liu, X.; Gao, A.; Dong, T.; Li, J.; Liu, J.; Jia, C. Regulation of charge carrier migration in Cu_2O/$W_{18}O_{49}$ S-scheme heterostructure for highly selective photocatalytic reduction of CO_2 to HCOOH in water. *Sep. Purif. Technol.* **2025**, *362*, 131791. DOI
76. Zhang, M.; Mao, Y.; Bao, X.; et al. Coupling benzylamine oxidation with CO_2 photoconversion to ethanol over a black phosphorus and bismuth tungstate S-scheme heterojunction. *Angew. Chem. Int. Ed. Engl.* **2023**, *62*, e202302919. DOI
77. Zhao, H.; Duan, J.; Zhang, Z.; Wang, W. S-scheme heterojunction and defect site engineering on Cu_xIn_5S-$Cu_{2-y}Se$ for highly efficient photoreduction of CO_2 to methanol. *ChemCatChem* **2022**, *14*, e202101733. DOI
78. Zhang, Y.; Dai, L.; Wang, X.; et al. S-scheme Bi_4TaO_8Cl/g-C_3N_4 heterostructure accelerates photocatalytic CO_2 reduction to CH_3OH. *Colloids. Surf. A. Physicochem. Eng. Asp.* **2026**, *735*, 139451. DOI
79. Bian, Y.; He, H.; Dawson, G.; Zhang, J.; Dai, K. In2O3/Bi19Br3S27 S-scheme heterojunction with enhanced photocatalytic CO2 reduction. *Sci. China. Mater.* **2024**, *67*, 514-23. DOI

80. Mao, Q.; Jiao, S.; Ren, K.; et al. Transition metal and phosphorus co-doping induced lattice strain in mesoporous Rh-based nanospheres for pH-universal hydrogen evolution electrocatalysis. *Chem. Eng. J.* **2021**, *426*, 131227. DOI
81. Singh, P. Synthesis of novel benzocoronene tetracarboxdiimides for fluorescent imaging of latent fingerprints. *J. Photoch. Photobio. A.* **2020**, *403*, 112824. DOI
82. Guo, Q.; Lu, F.; Tan, Q.; Zhou, T.; Xiong, J.; Zhang, W. Al_2O_3-based a-IGZO Schottky diodes for temperature sensing. *Sensors. (Basel).* **2019**, *19*, 224. DOI PubMed PMC
83. Jiang, P.; Wang, K.; Liu, W.; et al. Hot electrons induced by localized surface plasmon resonance in Ag/g-C_3N_4 Schottky junction for photothermal catalytic CO_2 reduction. *Polymers. (Basel).* **2024**, *16*, 2317. DOI PubMed PMC
84. Ma, Y.; Yi, X.; Wang, S.; et al. Selective photocatalytic CO_2 reduction in aerobic environment by microporous Pd-porphyrin-based polymers coated hollow TiO_2. *Nat. Commun.* **2022**, *13*, 1400. DOI PubMed PMC
85. Zhou, B.; Yang, Y.; Liu, Z.; et al. Boosting photocatalytic CO_2 reduction via Schottky junction with ZnCr layered double hydroxide nanoflakes aggregated on 2D $Ti_3C_2T_x$ cocatalyst. *Nanoscale* **2022**, *14*, 7538-46. DOI
86. Xu, G.; Chen, Y.; Lin, P.; Zhang, Z.; Ji, T.; Su, W. Construction of a 0D/2D Ni *x* P/$LaTiO_2$ N Schottky junction photocatalyst for efficient visible-light-driven photocatalytic CO_2 reduction. *Catal. Sci. Technol.* **2025**, *15*, 2027-33. DOI
87. Ma, S.; Yang, P.; Sun, H.; et al. Enhanced CO_2 photoreduction by constructing BiOCl/NiS Schottky heterojunction with a giant internal electric field. *Sep. Purif. Technol.* **2025**, *354*, 128976. DOI
88. Zhou, G.; Zhang, L.; Xia, Y.; et al. Highly selective photocatalytic CO_2 reduction by metal-N_4 dynamically generated from atomically dispersed copper. *Chem. Eng. J.* **2023**, *477*, 147040. DOI
89. Meng, M.; Wu, X.; Chai, Q.; et al. Enhanced interface coupling accelerates charge transfer of a MoO_{2-x}/Bi_2MoO_6 Schottky junction for CO_2 photoreduction to CH_4. *Rare. Metals.* **2025**, *44*, 10271-81. DOI
90. Zhu, Y.; Lin, L.; Zhou, M.; et al. Regulating the oxygen vacancies on the $Ti_3C_2T_x$/BiOCl Schottky heterojunction for highly efficient photoreduction of CO_2 to CH4. *Sep. Purif. Technol.* **2025**, *379*, 134865. DOI
91. Pan, L.; Qi, J.; Mei, H.; et al. Nearly 100% selectivity of photothermal CO2 reduction into CH_4 achieved by Pt/$Sr_2Nb_2O_7$ heterojunction. *Mater. Today. Nano.* **2023**, *22*, 100327. DOI
92. Zhang, M.; Wang, X.; Qi, X.; et al. Effect of Ag cocatalyst on highly selective photocatalytic CO_2 reduction to HCOOH over CuO/Ag/UiO-66 Z-scheme heterojunction. *J. Catal.* **2022**, *413*, 31-47. DOI
93. Guan, Q.; Chen, J.; Chen, D.; et al. A new sight on the catalytic oxidation kinetic behaviors of bamboo cellulose fibers under TEMPO-oxidized system: the fate of carboxyl groups in treated pulps. *J. Catal.* **2019**, *370*, 304-9. DOI
94. Yi, J.; Li, H.; Gong, Y.; et al. Phase and interlayer effect of transition metal dichalcogenide cocatalyst toward photocatalytic hydrogen evolution: The case of $MoSe_2$. *Appl. Catal. B. Environ.* **2019**, *243*, 330-6. DOI
95. Rhimi, B.; Zhou, M.; Yan, Z.; Cai, X.; Jiang, Z. Cu-based materials for enhanced C^{2+} product selectivity in photo-/electro-catalytic CO_2 reduction: challenges and prospects. *Nanomicro. Lett.* **2024**, *16*, 64. DOI PubMed PMC
96. Shang, X.; Li, G.; Wang, R.; Xie, T.; Ding, J.; Zhong, Q. Precision loading of Pd on Cu species for highly selective CO_2 photoreduction to methanol. *Chem. Eng. J.* **2023**, *456*, 140805. DOI
97. Du, H.; Gao, X.; Ma, Q.; Yang, X.; Zhao, T. S. Cu/PCN Metal-semiconductor heterojunction by thermal reduction for photoreaction of CO_2-Aerated H_2O to CH_3OH and C_2H_5OH. *ACS. Omega.* **2022**, *7*, 16817-26. DOI
98. Albo, J.; García, G. Enhanced visible-light photoreduction of CO_2 to methanol over Mo_2C/TiO_2 surfaces in an optofluidic microreactor. *React. Chem. Eng.* **2021**, *6*, 304-12. DOI
99. Cen, G.; Chu, W.; Lu, J.; Ding, J.; Hu, Y.; Wang, W. Boosting photocatalytic CO_2 reduction to CH_3OH on TiO_2 via AuCu alloy synergistic catalysis without sacrificial agent. *J. Environ. Chem. Eng.* **2026**, *14*, 121314. DOI
100. Chen, W.; Wu, S.; Xie, L.; et al. Surface selenation engineering on metal cocatalysts for highly efficient photoreduction of carbon dioxide to methanol. *Chem. Eng. J.* **2023**, *464*, 142612. DOI
101. Ban, C.; Wang, Y.; Feng, Y.; et al. Photochromic single atom Ag/TiO_2 catalysts for selective CO_2 reduction to CH_4. *Energy. Environ. Sci.* **2024**, *17*, 518-30. DOI
102. Chen, L.; Li, H.; Li, H.; et al. Accelerating photogenerated charge kinetics via the g-C_3N_4 Schottky junction for enhanced visible-light-driven CO_2 reduction. *Appl. Catal. B. Environ.* **2022**, *318*, 121863. DOI
103. Yin, S.; Zhao, X.; Jiang, E.; Yan, Y.; Zhou, P.; Huo, P. Boosting water decomposition by sulfur vacancies for efficient CO_2 photoreduction. *Energy. Environ. Sci.* **2022**, *15*, 1556-62. DOI
104. Bai, S.; Zhang, N.; Gao, C.; Xiong, Y. Defect engineering in photocatalytic materials. *Nano. Energy.* **2018**, *53*, 296-336. DOI

105. Maarisetty, D.; Baral, S. S. Defect engineering in photocatalysis: formation, chemistry, optoelectronics, and interface studies. *J. Mater. Chem. A.* **2020**, *8*, 18560-604. DOI
106. Zuo, C.; Tang, X.; Wang, H.; Su, Q. A Review of the effect of defect modulation on the photocatalytic reduction performance of carbon dioxide. *Molecules* **2024**, *29*, 2308. DOI PubMed PMC
107. Pastor, E.; Sachs, M.; Selim, S.; Durrant, J. R.; Bakulin, A. A.; Walsh, A. Electronic defects in metal oxide photocatalysts. *Nat. Rev. Mater.* **2022**, *7*, 503-21. DOI
108. Xiong, F.; Tan, S.; Yao, X.; An, Q.; Mai, L. Crystal defect modulation in cathode materials for non-lithium ion batteries: progress and challenges. *Mater. Today.* **2021**, *45*, 169-90. DOI
109. Li, R.; Li, T.; Zhou, Q. Impact of titanium dioxide TiO_2 modification on its application to pollution treatment - a review. *Catalysts* **2020**, *10*, 804. DOI
110. Zhan, F.; Wen, G.; Li, R.; et al. A comprehensive review of oxygen vacancy modified photocatalysts: synthesis, characterization, and applications. *Phys. Chem. Chem. Phys.* **2024**, *26*, 11182-207. DOI
111. Adormaa, B. B.; Darkwah, W. K.; Ao, Y. Oxygen vacancies of the TiO_2 nano-based composite photocatalysts in visible light responsive photocatalysis. *RSC. Adv.* **2018**, *8*, 33551-63. DOI PubMed PMC
112. Lee, G. R.; Song, K.; Hong, D.; et al. Unraveling oxygen vacancy-driven catalytic selectivity and hot electron generation on heterointerfaces using nanostructured platform. *Nat. Commun.* **2025**, *16*, 2909. DOI PubMed PMC
113. Hong, J.; Hu, Z.; Probert, M.; et al. Exploring atomic defects in molybdenum disulphide monolayers. *Nat. Commun.* **2015**, *6*, 6293. DOI PubMed PMC
114. Garcia-Esparza, A. T.; Park, S.; Abroshan, H.; et al. Local structure of sulfur vacancies on the basal plane of monolayer MoS_2. *ACS. Nano.* **2022**, *16*, 6725-33. DOI
115. Wang, R.; Zhang, M.; Liu, J.; et al. Defect-phase engineered NiTi-TiO_2 enabling near-unity selective photocatalytic CO_2-to-methanol conversion. *Nat. Commun.* **2025**, *16*, 7844. DOI PubMed PMC
116. Wang, J.; Liu, K.; Liao, W.; et al. Metal vacancies in semiconductor oxides enhance hole mobility for efficient photoelectrochemical water splitting. *Nat. Catal.* **2025**, *8*, 229-38. DOI
117. Liu, Z.; Wang, G.; Guo, J.; Wang, Y. Accurate construction of cobalt vacancies in Co_3O_4 to promote oxyhydroxide formation for water oxidation. *Sci. China. Mater.* **2024**, *67*, 780-7. DOI
118. Deng, H.; Zhu, X.; Chen, Z.; Zhao, K.; Cheng, G. Oxygen vacancy engineering of TiO_{2-x} nanostructures for photocatalytic CO_2 reduction. *Carbon. Lett.* **2022**, *32*, 1671-80. DOI
119. Kong, F.; Lu, X.; Xie, J.; Lu, Z.; Hu, J.; Cao, Y. Enhanced photocatalytic CO_2 reduction by controlled oxygen vacancy generation and co-constructed heterojunction strategy for Pd/CeO_2. *Inorg. Chem. Front.* **2024**, *11*, 2932-44. DOI
120. Guan, M.; Lu, N.; Zhang, X.; et al. Engineering of oxygen vacancy and bismuth cluster assisted ultrathin $Bi_{12}O_{17}Cl_2$ nanosheets with efficient and selective photoreduction of CO_2 to CO. *Carbon. Energy.* **2024**, *6*, e420. DOI
121. Cheng, S.; Sun, Z.; Lim, K. H.; et al. BiOCl nanoflowers with high levels of oxygen vacancy for photocatalytic CO_2 reduction. *ACS. Appl. Nano. Mater.* **2023**, *6*, 3608-17. DOI
122. Yang, Q.; Wang, Y.; Tian, Q.; et al. Enhancement effect of oxygen vacancy on photocatalytic CO_2 reduction. *J. Mater. Chem. A.* **2024**, *12*, 7207-14. DOI
123. Liu, H.; Chen, Y.; Wang, W.; et al. *In situ* solvothermal reduction engineering enables delicate control over surface-rich oxygen vacancies on Bi_2WO_6 for highly efficient photocatalytic CO_2 reduction. *EES. Catal.* **2023**, *1*, 495-503. DOI
124. Liu, X.; Yang, L.; Huang, M.; et al. Oxygen vacancy-regulated metallic semiconductor MoO_2 nanobelt photoelectron and hot electron self-coupling for photocatalytic CO_2 reduction in pure water. *Appl. Catal. B. Environ.* **2022**, *319*, 121887. DOI
125. Qian, Z.; Zhang, L.; Zhang, Y.; Cui, H. Synergistically boosting of CO_2 photoreduction over Bi/BiOBr nanostructure via *in-situ* formation of oxygen vacancy and metallic Bi. *Sep. Purif. Technol.* **2023**, *324*, 124581. DOI
126. Yu, B.; Wu, Y.; Meng, F.; et al. Formation of hierarchical Bi_2MoO_6/In_2S_3 S-scheme heterojunction with rich oxygen vacancies for boosting photocatalytic CO_2 reduction. *Chem. Eng. J.* **2022**, *429*, 132456. DOI
127. Zhang, Y.; Yao, D.; Xia, B.; et al. ReS_2 Nanosheets with *in situ* formed sulfur vacancies for efficient and highly selective photocatalytic CO_2 Reduction. *Small. Sci.* **2021**, *1*, 2000052. DOI PubMed PMC
128. Wang, F.; Jiang, R.; Sun, H.; Yao, S.; Wang, H.; Liu, L. Enhanced photocatalytic CO_2 reduction to CO performance by regulable surface active sulfur vacancies. *Sust. Chem. Energy. Mater.* **2025**, *2*, 100023. DOI
129. Gao, X.; Li, L.; Zhao, Z.; et al. Sulfur vacancy-rich ZnS on ordered microporous carbon frameworks for efficient photocatalytic CO_2 reduction. *Appl. Catal. B. Environ. Energy.* **2025**, *364*, 124835. DOI

130. Sun, T.; Zhao, P.; Zhou, Q.; Zhang, Y.; Li, Q.; Chen, C. γ-radiation induced deposition of au nanoparticles on defect-rich CdS for enhanced CO_2 photoreduction under visible light. *Water. Air. Soil. Pollut.* **2024**, *235*, 6975. DOI
131. Nie, Y.; Bo, T.; Zhou, W.; et al. Understanding the role of Zn vacancy induced by sulfhydryl coordination for photocatalytic CO_2 reduction on $ZnIn_2S_4$. *J. Mater. Chem. A.* **2023**, *11*, 1793-800. DOI
132. Xie, J.; Lu, Z.; Feng, Y.; et al. A small organic molecule strategy for remedying oxygen vacancies by bismuth defects in BiOBr nanosheet with excellent photocatalytic CO2 reduction. *Nano. Res.* **2024**, *17*, 297-306. DOI
133. Di, J.; Chen, C.; Zhu, C.; et al. Bismuth vacancy-tuned bismuth oxybromide ultrathin nanosheets toward photocatalytic CO_2 reduction. *ACS. Appl. Mater. Interfaces.* **2019**, *11*, 30786-92. DOI
134. Shi, X.; Dai, W.; Dong, X.; Ren, Q.; Sheng, J.; Dong, F. Dual Cu and S vacancies boost CO_2 photomethanation on $Cu_{1.95}S_{1-x}$: vacancy-regulated selective photocatalysis. *Appl. Catal. B. Environ.* **2023**, *339*, 123147. DOI
135. Guo, Z.; Shen, B.; Jiang, Z.; Wu, N.; You, Y. Effective near-infrared light-driven photocatalytic reduction of CO_2 by dual-site doped carbon nitrides. *Ind. Eng. Chem. Res.* **2024**, *63*, 18931-9. DOI
136. Ghuman, K. K.; Wood, T. E.; Hoch, L. B.; Mims, C. A.; Ozin, G. A.; Singh, C. V. Illuminating CO_2 reduction on frustrated Lewis pair surfaces: investigating the role of surface hydroxides and oxygen vacancies on nanocrystalline $In_2O_{3-x}(OH)_y$. *Phys. Chem. Chem. Phys.* **2015**, *17*, 14623-35. DOI
137. Yan, T.; Li, N.; Wang, L.; et al. Bismuth atom tailoring of indium oxide surface frustrated Lewis pairs boosts heterogeneous CO_2 photocatalytic hydrogenation. *Nat. Commun.* **2020**, *11*, 6095. DOI PubMed PMC
138. Ismail, A.; Zahid, M.; Ahmad, B.; et al. Tailoring g-C_3N_4 properties through P and K co-doping: advancing photocatalytic CO_2 reduction to CH_4. *Chem. Eng. J.* **2025**, *513*, 163023. DOI
139. Thambiliyagodage, C.; Usgodaarachchi, L. Photocatalytic activity of N, Fe and Cu co-doped TiO2 nanoparticles under sunlight. *Curr. Res. Green. Sustain. Chem.* **2021**, *4*, 100186. DOI
140. Zhang, J.; Wang, W.; Yang, Y.; Yan, Y.; Yan, Y.; Zhu, Z. N-doping of TiO_2 for enhanced CO_2 photocatalytic reduction and research on reaction mechanisms. *Carbon. Lett.* **2025**, *35*, 2215-26. DOI
141. Zhang, W.; Zhou, Q.; Li, N.; Li, M. Enhanced photocatalytic reduction of CO_2 into CH_4 over N, Eu co-doped TiO_2: Insight into the synergistic effect of N and Eu. *Appl. Catal. A-Gen.* **2023**, *650*, 118977. DOI
142. Peng, H.; Zhang, Q.; Fan, Z.; et al. A P-doped BiOBr nanosheet for enhanced photocatalytic CO_2 reduction efficiency. *J. Mol. Struct.* **2024**, *1307*, 138041. DOI
143. Song, X.; Liu, X.; Ren, Z.; et al. Insights into the greatly improved catalytic performance of N-doped BiOBr for CO_2 photoreduction. *Acta. Physico-Chimica. Sinica.* **2025**, *41*, 100055. DOI
144. Shen, M.; Cai, X.; Cao, B.; Cao, J.; Xu, Y. Boron-doped ultrathin BiOBr nanosheet promotion for photocatalytic reduction of CO_2 into CO. *J. Alloy. Compd.* **2024**, *981*, 173727. DOI
145. Xie, Y.; Wang, Y.; Zhou, Y.; et al. Cation exchange strategy to construct Co-doped BiOBr nanosheets for high-efficient photocatalytic CO_2 to CO. *Appl. Catal. A-Gen.* **2024**, *669*, 119504. DOI
146. Xiong, Y.; Luo, Y.; Qin, W.; et al. Europium doping into BiOBr to promote photogenerated electron-hole separation and enhance photocatalytic reduction of CO_2 to CO. *J. Rare. Earths.* **2026**, *44*, 2368-75. DOI
147. Fang, M.; Li, N.; Han, Y.; et al. Br self-doping enhances the piezo-photocatalysis of BiOBr for efficient CO_2 reduction and antibiotic degradation. *Chem. Eng. J.* **2025**, *524*, 169525. DOI
148. Pan, B.; Wu, Y.; Rhimi, B.; et al. Oxygen-doping of $ZnIn_2S_4$ nanosheets towards boosted photocatalytic CO_2 reduction. *J. Energy. Chem.* **2021**, *57*, 1-9. DOI
149. Zhou, F.; Zhang, Y.; Wu, J.; et al. Utilizing Er-doped $ZnIn_2S_4$ for efficient photocatalytic CO_2 conversion. *Appl. Catal. B. Environ.* **2024**, *341*, 123347. DOI
150. Wang, W.; Gu, S.; Guan, Y.; et al. Y-doped improved ZnIn2S4 promotes photocatalytic reduction of CO_2 reaction. *Mater. Today. Commun.* **2025**, *46*, 112624. DOI
151. Jiang, H.; Zhang, Y.; Zhou, F.; et al. Yb-doped $ZnIn_2S_4$ with S vacancies for photocatalytic reduction of CO_2 to CO. *J. Environ. Chem. Eng.* **2025**, *13*, 118709. DOI
152. Gao, X.; Zhao, J.; Song, H.; et al. Ionic liquid-assisted synthesis of P- and F-co-doped porous CN for boosting CO_2 photoreduction. *New. J. Chem.* **2025**, *49*, 18830-9. DOI
153. Huang, X.; Gu, W.; Hu, S.; et al. Phosphorus-doped inverse opal g-C_3N_4 for efficient and selective CO generation from photocatalytic reduction of CO_2. *Catal. Sci. Technol.* **2020**, *10*, 3694-700. DOI

154. Shi, X.; Zhang, Q.; Zhou, Y.; et al. Boosting charge transfer in Au-decorated B/K co-doped CN nanosheets towards enhanced photocatalytic CO_2 reduction. *Mater. Chem. Front.* **2023**, *7*, 2049-58. DOI
155. Tang, J.; Guo, R.; Pan, W.; Zhou, W.; Huang, C. Visible light activated photocatalytic behaviour of Eu (III) modified g-C_3N_4 for CO_2 reduction and H_2 evolution. *Appl. Surf. Sci.* **2019**, *467-468*, 206-12. DOI
156. Liang, J.; Tian, F.; Li, Y.; Wang, Y.; Yan, X.; Zhang, H. Single-atom Cu anchored phosphorus-doped graphitic carbon nitride for selective photocatalytic CO_2 reduction. *Environ. Res.* **2025**, *285*, 122324. DOI
157. Di, J.; Chen, C.; Yang, S. Z.; et al. Isolated single atom cobalt in Bi_3O_4Br atomic layers to trigger efficient CO_2 photoreduction. *Nat. Commun.* **2019**, *10*, 2840. DOI PubMed PMC
158. Shown, I.; Samireddi, S.; Chang, Y. C.; et al. Carbon-doped SnS_2 nanostructure as a high-efficiency solar fuel catalyst under visible light. *Nat. Commun.* **2018**, *9*, 169. DOI PubMed PMC
159. Zaera, F. Role of Metal Cocatalysts in the photocatalytic production of hydrogen from water revisited. *Energy. Fuels.* **2025**, *39*, 2422-34. DOI PubMed PMC
160. Dong, C.; Lian, C.; Hu, S.; et al. Size-dependent activity and selectivity of carbon dioxide photocatalytic reduction over platinum nanoparticles. *Nat. Commun.* **2018**, *9*, 1252. DOI PubMed PMC
161. Lee, S.; Lee, D. H.; Hong, Y. H. Heterogenized homogeneous catalysts for photoelectrochemical carbon dioxide reduction: a path toward ideal hybrid systems. *Energy. Mater.* **2026**, *6*, 600017. DOI
162. Wang, Q.; Yuan, Y.; Li, C.; et al. Carbon quantum dot-modified TiO_2/$SrTiO_3$ heterojunction for boosting photocatalytic CO_2 reduction. *Renewable. Energy.* **2024**, *231*, 120997. DOI
163. Guo, R. T.; Bi, Z. X.; Lin, Z. D.; et al. Carbon quantum dots-modified Z-scheme $Bi_{12}O_{17}Cl_2$/NiAl-LDH for significantly boosting photocatalytic CO_2 reduction. *J. Colloid. Interface. Sci.* **2022**, *627*, 343-54. DOI
164. Deore, P. S.; Gray, M. D.; Chung, A. J.; Manderville, R. A. Ligand-induced G-quadruplex Polymorphism: a DNA nanodevice for label-free Aptasensor platforms. *J. Am. Chem. Soc.* **2019**, *141*, 14288-97. DOI PubMed
165. Li, X.; Duan, M.; Deng, Z.; et al. Catalytic enantioselective synthesis of chiral tetraarylmethanes. *Nat. Catal.* **2020**, *3*, 1010-9. DOI
166. Zhang, Y.; Guo, F.; Wang, K.; et al. Precisely modulate interfacial Bi-O bridge bond in Co-TCPP/Bi_3O_4Br to trigger long-lasting charge separation for boosting CO_2 photoreduction. *Chem. Eng. J.* **2023**, *465*, 142663. DOI
167. Di, J.; Chen, C.; Zhu, C.; et al. Cobalt nitride as a novel cocatalyst to boost photocatalytic CO_2 reduction. *Nano. Energy.* **2021**, *79*, 105429. DOI
168. Meng, W.; Sui, X.; Liu, Y.; et al. Collaborative influence of Ni single atoms and oxygen defects on Bi_3O_4Br for boosting light-driven CO_2 hydrogenation to CH4. *Appl. Catal. B. Environ. Energy.* **2025**, *366*, 125033. DOI
169. Fu, H.; Tian, J.; Zhang, Q.; et al. Single-atom modified graphene cocatalyst for enhanced photocatalytic CO_2 reduction on halide perovskite. *Chin. J. Catal.* **2024**, *64*, 143-51. DOI
170. Zhou, M.; Wang, Z.; Mei, A.; et al. Photocatalytic CO_2 reduction using La-Ni bimetallic sites within a covalent organic framework. *Nat. Commun.* **2023**, *14*, 2473. DOI PubMed PMC
171. Roudsari, B. D.; Hasannia, S.; Kazemeini, M. Selective photocatalytic reduction of CO_2 to CO mediated by atomically dispersed Cu-anchored upon hollow covalent organic frameworks. , *102*, 103282. DOI
172. Wang, S.; Teramura, K.; Hisatomi, T.; et al. Dual Ag/Co cocatalyst synergism for the highly effective photocatalytic conversion of CO_2 by H_2O over Al-$SrTiO_3$. *Chem. Sci.* **2021**, *12*, 4940-8. DOI PubMed PMC
173. Pang, R.; Teramura, K.; Morishita, M.; Asakura, H.; Hosokawa, S.; Tanaka, T. Enhanced CO evolution for photocatalytic conversion of CO_2 by H_2O over Ca modified Ga_2O_3. *Commun. Chem.* **2020**, *3*, 137. DOI PubMed PMC
174. Hu, S.; Deng, Z.; Xing, M.; Wu, S.; Zhang, J. Construction of Cu cocatalyst on TiO_2 for regulating the selectivity of photocatalytic CO_2 reduction. *Res. Chem. Intermed.* **2022**, *48*, 3275-87. DOI
175. Pan, H.; Wang, X.; Xiong, Z.; Sun, M.; Murugananthan, M.; Zhang, Y. Enhanced photocatalytic CO_2 reduction with defective TiO_2 nanotubes modified by single-atom binary metal components. *Environ. Res.* **2021**, *198*, 111176. DOI
176. Xiong, Z.; Lei, Z.; Chen, X.; et al. CO_2 photocatalytic reduction over Pt deposited TiO_2 nanocrystals with coexposed {101} and {001} facets: effect of deposition method and Pt precursors. *Catal. Commun.* **2017**, *96*, 1-5. DOI
177. Li, L.; Dai, X.; Lu, M.; et al. Electron-enriched single-Pd-sites on g-C_3N_4 nanosheets achieved by in-situ anchoring twinned Pd nanoparticles for efficient CO_2 photoreduction. *Advanced. Powder. Materials.* **2024**, *3*, 100170. DOI
178. Huang, Z.; Sun, S.; Ma, M.; et al. Facile synthesis of TiO_2 supported Pd nanoparticles for efficient photocatalytic CO_2 reduction to CH_4 with H_2O. *Sustainable. Mater. Technol.* **2025**, *43*, e01247. DOI

179. Bashal, A. H.; Alkanad, K.; Al-ghorbani, M.; Ben, Aoun. S.; Bajiri, M. A. Synergistic effect of cocatalyst and S-scheme heterojunction over 2D/2D g-C_3N_4/MoS_2 heterostructure coupled Cu nanoparticles for selective photocatalytic CO_2 reduction to CO under visible light irradiation. *J. Environ. Chem. Eng.* **2023**, *11*, 109545. DOI
180. Hu, B.; Li, Z.; Wang, B.; et al. Construction of Co-In dual single-atom catalysts for photocatalytic CO_2 reduction into CH_4. *Appl. Catal. B. Environ. Energy.* **2025**, *371*, 125196. DOI
181. Zhao, X.; Guan, J.; Li, J.; et al. CeO_2/3D g-C_3N_4 heterojunction deposited with Pt cocatalyst for enhanced photocatalytic CO_2 reduction. *Appl. Surf. Sci.* **2021**, *537*, 147891. DOI
182. Mu, X.; Xu, Q.; Xie, Y.; et al. Hollow cubic TiO_2 loaded with copper and gold nanoparticles for photocatalytic CO_2 reduction. *J. Alloy. Compd.* **2024**, *980*, 173589. DOI
183. Li, N.; Geng, D.; Zhou, J. Ag and Cu nanoparticles synergistically enhance photocatalytic CO_2 reduction activity of B phase TiO_2. *Catal. Lett.* **2022**, *152*, 124-38. DOI
184. Wang, L.; Xiong, J.; Yu, X.; et al. Synergistic integration of Au-Ag alloy nanoparticles with TiO_2 for efficient photocatalytic CO_2 reduction. *J. Environ. Chem. Eng.* **2025**, *13*, 119971. DOI
185. Dai, F.; Zhang, M.; Han, J.; et al. Bifunctional core-shell co-catalyst for boosting photocatalytic CO_2 reduction to CH_4. *Nano. Res.* **2024**, *17*, 1259-66. DOI
186. Bai, Y.; Yang, P.; Wang, L.; et al. Ultrathin $Bi_4O_5Br_2$ nanosheets for selective photocatalytic CO_2 conversion into CO. *Chem. Eng. J.* **2019**, *360*, 473-82. DOI
187. Zhou, L.; Xu, J.; Wei, S.; Liu, L.; Zhou, Z.; Liu, X. Fabrication of NiFe-LDH/MoS_2 2D/2D material to construct direct Z-scheme heterojunction for enhanced C_2O photocatalytic reduction under visible light irradiation. *Carbon. Capture. Sci. Technol.* **2024**, *12*, 100223. DOI
188. Yang, C.; Tan, Q.; Li, Q.; et al. 2D/2D Ti_3C_2 MXene/g-C_3N_4 nanosheets heterojunction for high efficient CO_2 reduction photocatalyst: dual effects of urea. *Appl. Catal. B. Environ. Energy.* **2020**, *268*, 118738. DOI
189. Jo, W.; Moru, S.; Tonda, S. A green approach to the fabrication of a TiO_2/NiAl-LDH core-shell hybrid photocatalyst for efficient and selective solar-powered reduction of CO_2 into value-added fuels. *J. Mater. Chem. A.* **2020**, *8*, 8020-32. DOI
190. Guo, S.; Guo, R.; Zhang, Z.; et al. Core-shell structured Cu_2O@NiAl-LDH/CQDs photocatalysts for efficient photocatalytic reduction of CO_2 to C_2 products. *Sep. Purif. Technol.* **2025**, *354*, 129449. DOI
191. Li, Z.; Xiong, J.; Huang, Y.; et al. Synergy mechanism of confined effect and Z-scheme electron transfer in core-shell structure photocatalyst for boosting photoreduction CO_2 activity. *Chem. Eng. J.* **2024**, *486*, 150304. DOI
192. Sayed, M.; Xu, F.; Kuang, P.; et al. Sustained CO_2-photoreduction activity and high selectivity over Mn, C-codoped ZnO core-triple shell hollow spheres. *Nat. Commun.* **2021**, *12*, 4936. DOI PubMed PMC
193. Wang, M.; Chen, D.; Lu, J. Recent advances in the construction of structurally diverse catalysts for enhanced photocatalytic CO_2 reduction. *Sep. Purif. Technol.* **2024**, *343*, 126917. DOI
194. Zheng, Z.; Du, T.; Chen, P.; et al. 2D/1D nested hollow porous $ZnIn_2S_4$/g-C_3N_4 heterojunction based on morphology modulation for photocatalytic CO_2 reduction. *J. Environ. Chem. Eng.* **2024**, *12*, 112971. DOI
195. Dehkordi A, Ziarati A, Ghasemi JB, Badiei A. Preparation of hierarchical g-C_3N_4@TiO_2 hollow spheres for enhanced visible-light induced catalytic CO_2 reduction. *Solar. Energy.* **2020**, *205*, 465-73. DOI
196. Guan, Z.; Chen, Y.; Ding, Y.; et al. Efficient charge transfer and CO_2 photoreduction of hierarchical CeO_2@SnS_2 heterostructured hollow spheres with spatially separated active sites. *Appl. Surf. Sci.* **2022**, *592*, 153192. DOI
197. Lee, D.; Devthade, V.; Abraham, B. M.; Jo, W.; Tonda, S. An S-scheme heterointerface-engineered high-performance ternary NiAl-LDH@TiO_2/Ti_3C_2 MXene photocatalytic system for solar-powered CO_2 reduction to produce energy-rich fuels. *Chem. Eng. J.* **2024**, *480*, 148227. DOI
198. Li, Q.; He, L.; Zeng, Y.; Zhao, Y.; Ding, M. CdS-assisted ultrathin porous nitrogen-vacancy carbon nitride nanosheets for visible-light photocatalytic CO_2 reduction. *Carbon* **2023**, *214*, 118384. DOI
199. Liu, C.; Zhang, Y.; Shi, T.; Liang, Q.; Chen, Z. Hierarchical hollow-microsphere cadmium sulfide-carbon dots composites with enhancing charge transfer efficiency for photocatalytic CO_2 reduction. *J. Alloy. Compd.* **2023**, *936*, 168286. DOI
200. Mu, Y.; Zhao, J.; Wu, L.; et al. Lead-free halide perovskite hollow nanospheres to boost photocatalytic activity for CO_2 reduction. *Appl. Catal. B. Environ.* **2023**, *338*, 123024. DOI
201. Meng, J.; Jin, X.; Zhao, M.; et al. Construction of core-shell $Bi_4O_5Br_2$ structure for efficient photocatalytic CO_2 reduction. *Vacuum* **2025**, *233*, 114022. DOI

202. Gong, S.; Niu, Y.; Liu, X.; et al. Fabrication of hetero-metal oxide $NiCo_2V_2O_8$ hollow nanospheres for efficient visible light-driven CO_2 photoreduction. *Appl. Catal. B. Environ.* **2022**, *316*, 121663. DOI
203. Zhou, D.; Zhang, J.; Jin, Z.; Di, T.; Wang, T. Reduced graphene oxide assisted g-C_3N_4/rGO/NiAl-LDHs type II heterostructure with high performance photocatalytic CO_2 reduction. *Chem. Eng. J.* **2022**, *450*, 138108. DOI
204. Zhao, L.; Hou, H.; Wang, L.; et al. Atomic-level surface modification of ultrathin Bi_2WO_6 nanosheets for boosting photocatalytic CO_2 reduction. *Chem. Eng. J.* **2024**, *480*, 148033. DOI
205. Zhang, Y.; Liu, S.; Guo, X.; Mikulčić, H.; Xiao, R.; Wang, X. F-doped Bi_2MoO_6 nanosheets for photoreduction of CO_2 with H_2O. *J. Photoch. Photobio. A.* **2024**, *447*, 115278. DOI
206. Wang, Z.; Chen, Y.; Zhang, L.; Cheng, B.; Yu, J.; Fan, J. Step-scheme CdS/TiO_2 nanocomposite hollow microsphere with enhanced photocatalytic CO_2 reduction activity. *J. Mater. Sci. Technol.* **2020**, *56*, 143-50. DOI
207. Ma, D.; Bao, R.; Wang, J.; et al. Hyperdispersed and highly stable Bi single atom doped core-shell CuO for efficient photocatalytic CO_2 reduction via modulation of electronic structure. *Mater. Today. Energy.* **2025**, *53*, 102004. DOI
208. Zhao, T.; Cheng, G.; Zhang, W.; Xiong, J. Cocatalysts engineering promotes photocatalytic CO_2 reduction of hollow TiO_2 nanospheres: From Cu nanoparticles to CuAg species. *J. Alloy. Compd.* **2025**, *1010*, 177677. DOI
209. Wang, Y.; Zhang, L.; Zhang, X.; et al. Openmouthed β-SiC hollow-sphere with highly photocatalytic activity for reduction of CO_2 with H_2O. *Appl. Catal. B. Environ.* **2017**, *206*, 158-67. DOI
210. Zhang, Y.; Wu, Y.; Wan, L.; et al. Hollow core-shell Co_9S_8@$ZnIn_2S_4$/CdS nanoreactor for efficient photothermal effect and CO_2 photoreduction. *Appl. Catal. B. Environ.* **2022**, *311*, 121255. DOI
211. Zhou, H.; Wang, Y.; Wu, J.; et al. Enhanced photocatalytic reduction of CO_2 using a novel 2D/0D SnS_2/CeO_2 binary photocatalyst with Z-scheme heterojunction and oxygen vacancy. , *76*, 102591. DOI
212. Wu, P.; Wang, Q.; Xue, Q.; Xie, X.; Xia, L.; Wang, T. Enhancing photocatalytic CO_2 reduction via S-scheme heterojunctions with tuned band structure and enhanced built-in electric field. *J. Environ. Chem. Eng.* **2025**, *13*, 119778. DOI
213. Zhang, P.; Wang, S.; Guan, B. Y.; Lou, X. W. Fabrication of CdS hierarchical multi-cavity hollow particles for efficient visible light CO_2 reduction. *Energy. Environ. Sci.* **2019**, *12*, 164-8. DOI
214. Li, R.; Feng, P.; Li, B.; et al. Photocatalytic reduction of CO_2 over porous ultrathin NiO nanosheets with oxygen vacancies. *Chin. J. Catal.* **2025**, *73*, 242-51. DOI
215. Li, X.; Sun, B.; Fan, H.; et al. Oxygen vacancy-rich $Ni_2P_2O_7$ modified g-C_3N_4 heterojunction for highly-efficient CO_2 photoreduction. *Chem. Eng. J.* **2024**, *500*, 157174. DOI
216. Yu, H.; Chen, F.; Li, X.; et al. Synergy of ferroelectric polarization and oxygen vacancy to promote CO_2 photoreduction. *Nat. Commun.* **2021**, *12*, 4594. DOI PubMed PMC
217. Collado, L.; Reynal, A.; Fresno, F.; et al. Unravelling the effect of charge dynamics at the plasmonic metal/semiconductor interface for CO_2 photoreduction. *Nat. Commun.* **2018**, *9*, 4986. DOI PubMed PMC
218. Butler, K. T.; Davies, D. W.; Cartwright, H.; Isayev, O.; Walsh, A. Machine learning for molecular and materials science. *Nature* **2018**, *559*, 547-55. DOI PubMed
219. Mai, H.; Le, T. C.; Chen, D.; Winkler, D. A.; Caruso, R. A. Machine learning for electrocatalyst and photocatalyst design and discovery. *Chem. Rev.* **2022**, *122*, 13478-515. DOI
220. Hamoud H, Wolski L, Pankin I, Bañares MA, Daturi M, El-Roz M. *In. situ.* , *380*, 37. DOI PubMed
221. Behroozi, A. H.; Xu, R. Photocatalytic CO_2 reduction: photocatalysts, membrane reactors, and hybrid processes. *Chem. Catalysis.* **2023**, *3*, 100550. DOI
222. Dilla, M.; Becerikli, A. E.; Jakubowski, A.; Schlögl, R.; Ristig, S. Development of a tubular continuous flow reactor for the investigation of improved gas-solid interaction in photocatalytic CO_2 reduction on TiO_2. *Photochem. Photobiol. Sci.* **2019**, *18*, 314-8. DOI PubMed